

The Mac1 ADP-ribosylhydrolase is a Therapeutic Target for SARS-CoV-2

Rahul K. Suryawanshi^{1,*}, Priyadarshini Jaishankar^{2,*}, Galen J. Correy^{3,*}, Moira M. Rachman^{2,*}, Patrick C. O'Leary^{4,*}, Taha Y. Taha^{1,5,*}, Francisco J. Zapatero-Belinchón¹, Maria McCavitt-Malvido¹, Yagmur U. Doruk⁴, Maisie G. V. Stevens⁴, Morgan E. Diolaiti⁴, Manasi P. Jogalekar⁴, Alicia L. Richards^{5,6,7}, Mauricio Montano¹, Julia Rosecrans¹, Michael Matthay⁸, Takaya Togo², Ryan L. Gonciarz², Saumya Gopalkrishnan⁵, R. Jeffrey Neitz^{2,9}, Nevan J. Krogan^{3,5,7}, Danielle L. Swaney^{5,6,7}, Brian K. Shoichet², Melanie Ott^{1,8,10,#}, Adam R. Renslo^{2,#}, Alan Ashworth^{4,#}, James S. Fraser^{3,#}

¹ Gladstone Institute of Virology, Gladstone Institutes, San Francisco, CA

² Department of Pharmaceutical Chemistry, University of California San Francisco, San Francisco, CA

³ Department of Bioengineering and Therapeutic Sciences, University of California San Francisco, San Francisco, CA

⁴ Helen Diller Family Comprehensive Cancer Center, University of California San Francisco, San Francisco, CA

⁵ Quantitative Biosciences Institute (QBI), University of California San Francisco, San Francisco, CA

⁶ Department of Cellular and Molecular Pharmacology, University of California San Francisco, San Francisco, CA

⁷ Data Science and Biotechnology Institute, Gladstone Institutes, San Francisco, CA

⁸ Department of Medicine, University of California San Francisco, San Francisco, CA

⁹ Small Molecule Discovery Center, University of California San Francisco, San Francisco, CA

¹⁰ Chan Zuckerberg Biohub- San Francisco, San Francisco, CA

* These authors contributed equally

Corresponding authors (melanie.ott@gladstone.ucsf.edu, adam.renslo@ucsf.edu, alan.ashworth@ucsf.edu, jfraser@fraserlab.com)

Abstract

SARS-CoV-2 continues to pose a threat to public health. Current therapeutics remain limited to direct acting antivirals that lack distinct mechanisms of action and are already showing signs of viral resistance. The virus encodes an ADP-ribosylhydrolase macrodomain (Mac1) that plays an important role in the coronaviral lifecycle by suppressing host innate immune responses. Genetic inactivation of Mac1 abrogates viral replication *in vivo* by potentiating host innate immune responses. However, it is unknown whether this can be achieved by pharmacologic inhibition and can therefore be exploited therapeutically. Here we report a potent and selective lead small molecule, AVI-4206, that is effective in an *in vivo* model of SARS-CoV-2 infection. Cellular models indicate that AVI-4206 has high target engagement and can weakly inhibit viral replication in a gamma interferon- and Mac1 catalytic activity-dependent manner; a stronger antiviral effect for AVI-4206 is observed in human airway organoids. In an animal model of severe SARS-CoV-2 infection, AVI-4206 reduces viral replication, potentiates innate immune responses, and leads to a survival benefit. Our results provide pharmacological proof of concept that Mac1 is a valid therapeutic target via a novel immune-restoring mechanism that could potentially synergize with existing therapies targeting distinct, essential aspects of the coronaviral life cycle. This approach could be more widely used to target other viral macrodomains to develop antiviral therapeutics beyond COVID-19.

43 Introduction

44 Severe acute respiratory syndrome coronavirus 2 (SARS-CoV-2) continues to be a major threat to public
45 health. Despite the approval of several biologic and small molecule therapeutics, there is an urgent need for
46 new small molecule antivirals with distinct mechanisms of action to overcome potential resistance to existing
47 agents (Li et al. 2023b; von Delft et al. 2023). While most antivirals target an essential aspect of viral entry or
48 replication, a potential avenue for new antivirals with alternative mechanisms is to target viral proteins that
49 act to blunt the host immune response (Minkoff and tenOever 2023). For example, SARS-CoV-2 has evolved
50 multiple mechanisms to evade and counter interferon signaling (Kim and Shin 2021). The viral proteins
51 involved in such evasion would be valuable drug targets if their inhibition renders the host immune response
52 sufficient to control virus replication and reduce disease severity.

53
54 The macrodomain (Mac1) of non-structural protein 3 (NSP3) in SARS-CoV-2 is one such target that plays an
55 antagonistic role to the host interferon response (Schuller et al. 2023). Macrodomains are found across the
56 tree of life and catalyze the hydrolysis of ADP-ribose covalent modifications on protein side chains (Dasovich
57 and Leung 2023). Viral macrodomains are found in alphaviruses, hepatitis E virus, and many
58 betacoronaviruses (Leung et al. 2022) and in some systems, like murine hepatitis virus (MHV), their activity
59 can be essential for viral replication (Voth et al. 2021). While SARS-CoV-2 bearing either catalytically
60 inactivating point mutations (Taha et al. 2023b) or deletion of the Mac1 domain (Alhammad et al. 2023) have
61 minor phenotypes in cell culture, their replication is profoundly attenuated in animal models. This discordance
62 likely reflects the inability of cellular models to recapitulate the complex intercellular and systemic signaling
63 required for proper viral-host immune interactions. The underlying mechanism of action results from the
64 enzymatic activity of Mac1, which counters the wave of ADP-ribosylation that is catalyzed by poly-adenosine
65 diphosphate-ribose polymerase (PARP) proteins during the interferon response (Kerr et al. 2023; Kar et al.
66 2024; Parthasarathy et al. 2024). While the critical proteins and sites modified by interferon-induced PARPs
67 are not fully characterized, the inhibition of Mac1 should allow ADP-ribosylation and the resulting downstream
68 signaling to persist (Kar et al. 2024). Indeed, multiple interferon genes are down-regulated upon infection with
69 wild-type SARS-CoV-2 relative to a Mac1 deficient mutant, consistent with the hypothesis that antiviral
70 interferon signaling could be productively enhanced by Mac1 inhibition (Alhammad et al. 2023; Taha et al.
71 2023b).

72
73 We (Schuller et al. 2021; Gahbauer et al. 2023), and others (O'Connor et al. 2023; Schuller et al. 2023; Wazir
74 et al. 2024), have previously developed inhibitors of Mac1 with activity *in vitro*. However, the therapeutic
75 hypothesis that pharmacological Mac1 inhibition would restore host immune responses and lead to a survival
76 benefit after SARS-CoV-2 infection has not yet been tested. Here, we build on our experimental fragment
77 (Schuller et al. 2021) and virtual screening approach (Gahbauer et al. 2023) with medicinal chemistry, to
78 develop a potent lead compound, AVI-4206, that engages Mac1 in cellular models and has suitable
79 pharmacological properties to test antiviral efficacy *in vivo*. In an animal model of SARS-CoV-2 infection, AVI-
80 4206 reduces viral replication, restores an interferon response, and leads to a survival benefit. Therefore, our
81 results validate Mac1 as a therapeutic target via a novel immune-restoring mechanism that could synergize
82 with existing therapies targeting essential aspects of viral replication. The approach could be more widely
83 used to target other macrodomains in viruses beyond SARS-CoV-2.

84

85 Results

86 Optimization of *in vitro* potency against the SARS-CoV-2 Macrodomain

87 Previously, we described two novel Mac1 inhibitors, AVI-92 and AVI-219 (Gahbauer et al. 2023), which
88 evolved from fragment screening and virtual screening hits, respectively. Their potency was determined using
89 an ADPr-conjugated peptide displacement-based homogeneous time resolved fluorescence (HTRF) assay
90 (**Figure 1**). The superposition of the Mac1 crystal structures in complex with both leads inspired a parallel
91 approach to optimization, which was supported by additional high resolution X-ray structures of the complexes
92 (**Figure 1A,E, Supplementary Table 1, Supplementary Figure 1**). First, we generated a merged compound

93 that used the urea function of AVI-92 in the more lead-like AVI-219 scaffold, thus avoiding the phenolic and
94 carboxylate functionalities present in AVI-92. Indeed, the X-ray structure of the resulting complex between
95 Mac1 and AVI-4051 shows that it preserves and favorably orients the two hydrogen bonding contacts with
96 the carboxylate of Asp22 and exhibits a ~four-fold lower IC₅₀ value as compared to AVI-219 in the HTRF
97 assay (**Figure 1B,E**). Further structure activity relationship (SAR) studies revealed a strong preference for
98 urea (e.g., AVI-1500, IC₅₀ of ~120 nM) over acetamide (AVI-1501) or carbamate (AVI-3367) in productively
99 engaging Asp22 (**Figure 1B,E**).

100
101 Second, at the other end of the adenosine site, we observed that the pyrrolidinone carbonyl of AVI-219 could
102 accept hydrogen bonds from the backbone amides of Phe156/Asp157 (**Figure 1C,E**). To improve contacts
103 with non-polar residues in this sub-site, we next explored substitutions of the pyrrolidinone ring. While C-5
104 substituents as large as phenyl were tolerated (AVI-3762 and AVI-3763), these analogs showed reduced
105 ligand efficiency compared to AVI-219. By contrast, a methyl group at C-5 in either stereochemical
106 configuration (AVI-3764 and AVI-3765) improved potency and ligand efficiency. Introducing two methyl
107 groups at C-5 afforded the achiral, gem-dimethyl pyrrolidinone AVI-4636 with an impressive five-fold
108 improvement in potency (IC₅₀ of ~200 nM) compared to AVI-219 (**Figure 1C,E**).

109
110 Ultimately, combining the ethyl urea side chain of AVI-1500 with the gem-dimethyl pyrrolidinone of AVI-4636
111 produced AVI-4206, the most potent Mac1 inhibitor identified from this series, with an IC₅₀ value of ~20 nM
112 (**Figure 1A,E**). This potency approaches the floor of our HTRF assay, which uses 12 nM of enzyme, and
113 indicates that AVI-4206 is at least ~25-100-fold more potent than the AVI-92 and AVI-219 starting points,
114 respectively. The high resolution co-crystal structure of AVI-4206 confirmed that the desired interaction
115 elements and conformations were maintained from the separate optimization paths (**Figure 1e**). To confirm
116 that the high affinity binding of AVI-4206 was reflected in inhibition of Mac1 catalytic activity, we used auto
117 ADP-ribosylated PARP10 and a coupled NudT5/AMP-Glo assay to measure ADP-ribose released by the
118 enzymatic reaction (Kasson et al. 2021) (**Supplementary Figure 2**). This assay demonstrated AVI-4206
119 potently inhibits Mac1 with an IC₅₀ of 64 nM (**Figure 1D**).

100
101
102
103
104
105
106
107
108
109
110
111
112
113
114
115
116
117
118
119
120

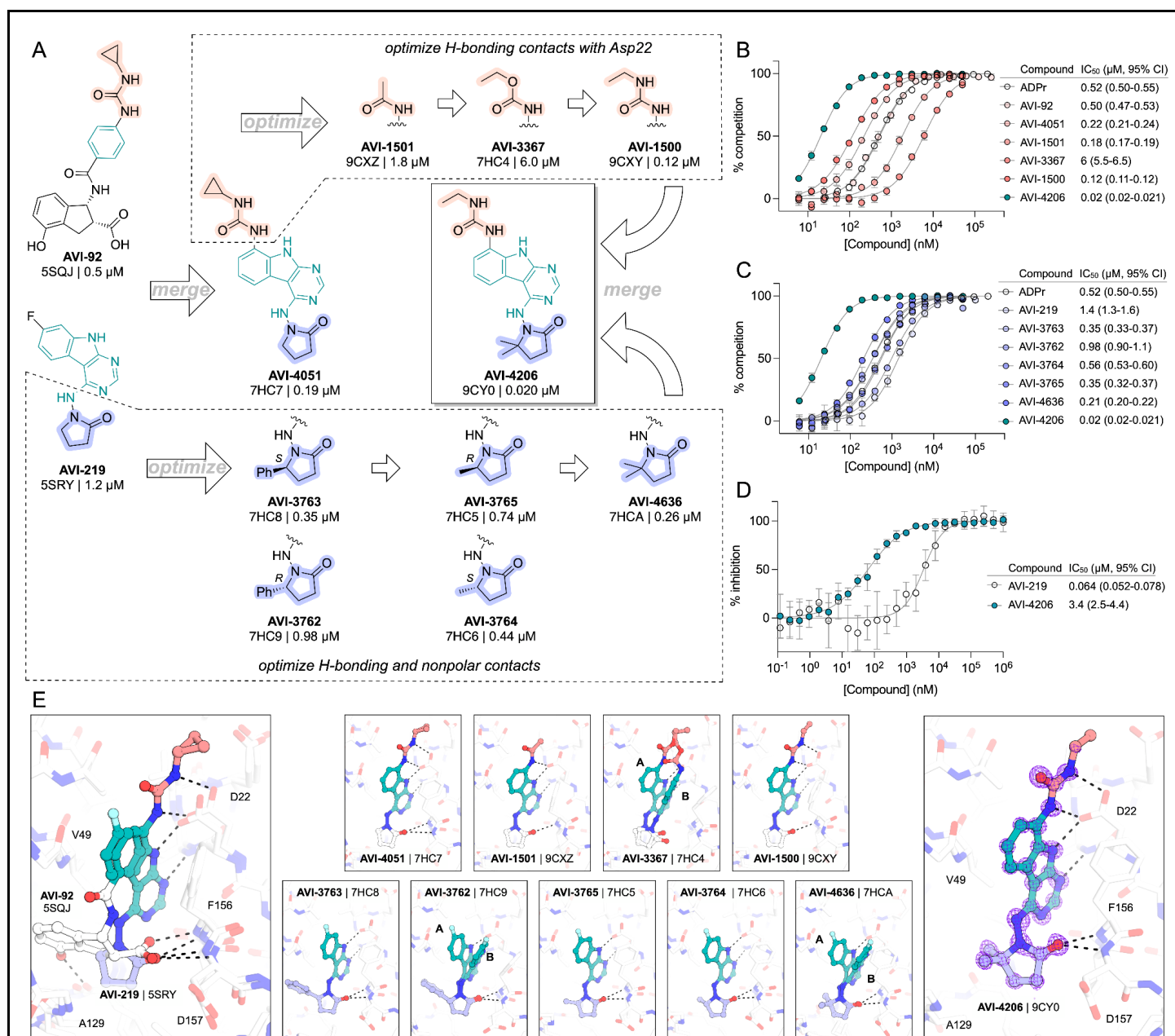


Figure 1: Iterative structure-based design and optimization of AVI-4206 activity against Mac1.

(A) Evolution of the early lead AVI-219 to AVI-4206 by introducing and optimizing urea functionality as found in AVI-92 to contact Asp22 and introducing geminal dimethyl substitution of the pyrrolidinone ring. HTRF-based IC₅₀ values from (B) and (C), and PDB codes from (E) are indicated.

(B and C) HTRF-based dose response curves showing peptide displacement of an ADPr-conjugated peptide from Mac1 by compounds from the urea (B) and the pyrrolidinone ring (C) optimization paths. Data is plotted as % competition mean ± SD of three technical replicates. Data were fitted with a sigmoidal dose-response equation using non-linear regression and the IC₅₀ values are quoted with 95% confidence intervals.

(D) Mac1 catalytic activity dose response curve for indicated compounds. Data is plotted as % inhibition mean ± SD of four technical replicates. IC₅₀ values are quoted with 95% confidence intervals.

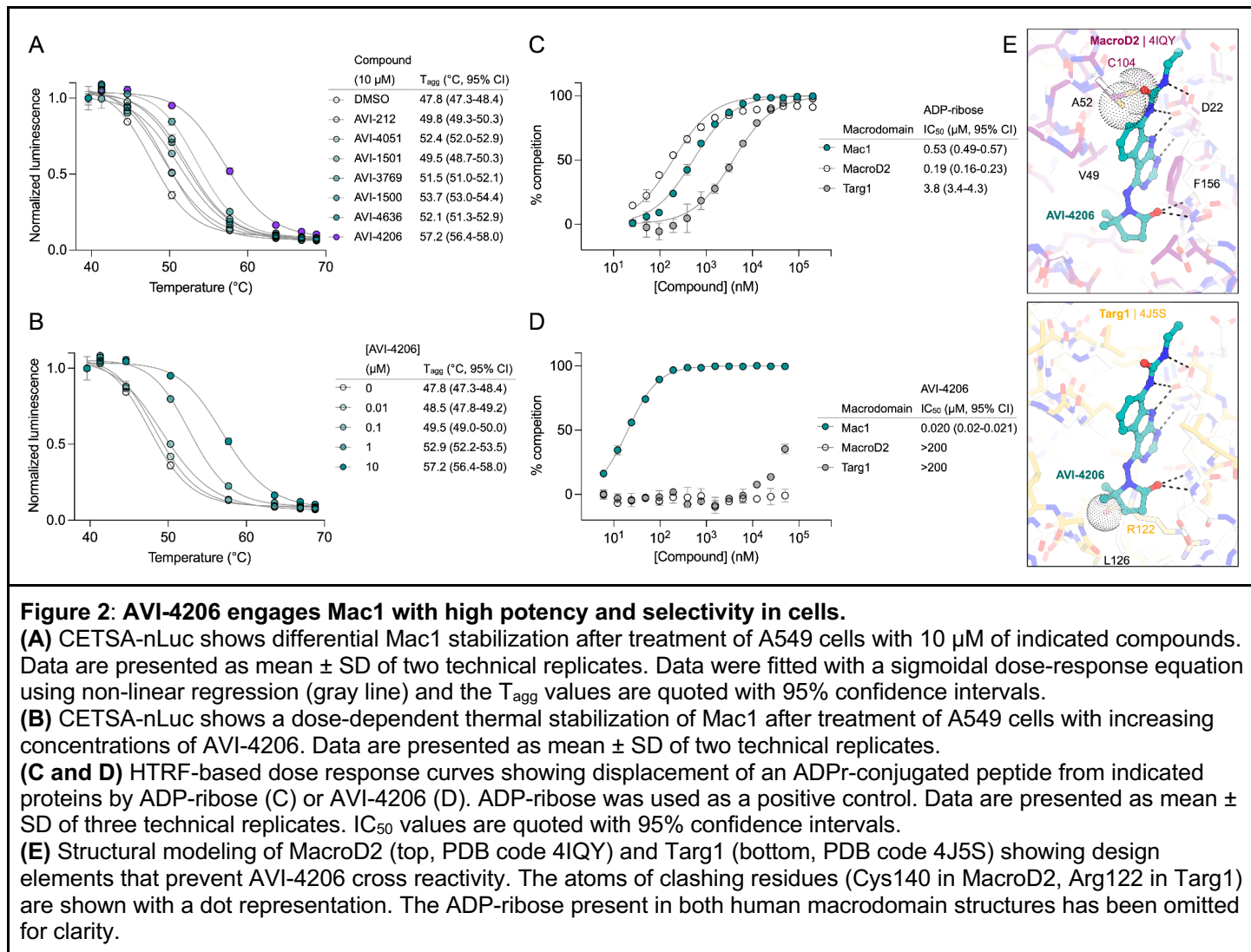
(E) X-ray structures indicating conserved interactions during the optimization path from AVI-92 and AVI-219 (left) to AVI-4206 (right). Structures of compounds from the urea and the pyrrolidinone ring optimization paths are presented in the top and bottom middle panels, respectively. Multiple ligand conformations were observed for AVI-3367, AVI-3762 and AVI-4636 (labeled A and B). The F_O-F_C difference electron density map calculated prior to ligand modeling is shown for AVI-4206 (purple mesh contoured at 5 σ). Electron density maps used to model ligand other ligands are shown in **Supplementary Figure 1**.

121

122 AVI-4206 engages Mac1 in cells with high specificity

123 Having discovered AVI-4206 as a potent inhibitor of Mac1, we next determined whether this compound could
124 enter cells and bind to Mac1 in this context. Therefore, to assess cellular target engagement, we developed
125 a nanoluciferase-based CELLular Thermal Shift Assay (CETSA-nLuc) assay (Martinez et al. 2018) to measure
126 thermal stabilization of Mac1 upon compound binding. A549 cells transiently expressing a HiBiT- and FLAG-
127 tagged Mac1 protein were treated with compounds for 1 hour and then incubated across a gradient of
128 temperatures. After heat exposure, cells were lysed and incubated with LgBiT protein which binds to soluble
129 HiBiT-Mac1 protein reconstituting nanoluciferase and producing a luminescent signal. We observed that the
130 T_{agg} (the temperature at which 50% of protein is soluble) shift for compounds at 10 μ M mirrored the affinities
131 measured by the HTRF assay, suggesting a dominant role for Mac1 affinity, rather than bioavailability, or
132 another factor, in determining target engagement in cells (**Figure 2A**). Furthermore, we observed a dose-
133 dependent shift in T_{agg} by AVI-4206, with a marked $\sim 10^{\circ}\text{C}$ shift in cells treated with 10 μ M of compound
134 compared to DMSO-treated control cells (**Figure 2B**). The observations were also validated by western
135 blotting with a FLAG-specific antibody (**Supplementary Figure 3**).
136

137 After confirming Mac1 target engagement in cells, we next tested the selectivity of AVI-4206 for Mac1 over
138 two human macrodomains, Targ1 and MacroD2. In an adapted HTRF assay, both human proteins bind to
139 ADP-ribose in the same low- μ M range as Mac1 (**Figure 2C**), AVI-4206 does not bind appreciably to either
140 protein in this assay (**Figure 2D**). The selectivity of AVI-4206 for the active site of Mac1 can be rationalized
141 by the presence of larger residues at key positions in the binding pocket in the human orthologs. In Targ1,
142 Cys104 occupies the analogous position to Ala52 of Mac1, leading to a putative clash with the urea moiety
143 (**Figure 2E**). Similarly, in MacroD2, Arg122 occupies the analogous position to Leu 126; both the larger
144 arginine side chain and accompanying backbone shift are predicted to clash with the gem-dimethyl of AVI-
145 4206 (**Figure 2E**). Due to the shared adenosine motif in the substrates for macrodomains and kinases, and
146 the therapeutic importance of protein kinases, we assessed AVI-4206 at 10 μ M against a panel of diverse
147 kinases and found no inhibition $>35\%$ (**Supplementary Table 2**). Lastly, we used mass spectrometry-based
148 thermal proteome profiling (TPP) (Savitski et al. 2014) to evaluate the selectivity of AVI-4206 against a
149 complex proteome. We added 50 nM recombinant Mac1 protein into cellular lysates from A549 cells that were
150 treated either with DMSO or with 100 μ M of AVI-4206. We find that Mac1, but no native protein from the A459
151 lysate, displays a statistically significant shift in melting temperature (3.02°C , adjusted P value = 0.045)
152 (**Supplementary Figure 4**). Collectively, these results indicate that AVI-4206 can cross cellular membranes
153 and engage with high specificity for Mac1.
154
155



156

157 AVI-4206 displays limited efficacy in cellular models

158 To determine whether AVI-4206 can inhibit viral replication in cellular models of SARS-CoV-2 infection, we
 159 treated IFN-deficient Vero cells stably expressing TMPRSS2 (Vero-TMPRSS2) and IFN-competent A549
 160 cells stably expressing high levels of ACE2 (A549-ACE2^h) with AVI-4206 and infected them with an mNeon
 161 reporter SARS-CoV-2 WA1 strain (Xie et al. 2020). We observed that treatment with AVI-4206 did not reduce
 162 viral replication in Vero-TMPRSS2 or A549-ACE2^h cells (**Figure 3A,B**), consistent with previous studies
 163 showing that Mac1 deficient SARS-CoV-2 can replicate efficiently in several cell lines ((Alhammad et al. 2023;
 164 Taha et al. 2023b)). This result stands in contrast to a SARS-CoV-2 protease inhibitor, nirmaltrevir, which
 165 potently inhibited replication in both cell lines (EC_{50} 275 nM and 9.4 nM, respectively) (**Figure 3A,B**).
 166 Nonetheless, this experiment, together with a viability assay, indicated no direct cytotoxicity of AVI-4206 at
 167 concentrations as high as 100 μM (**Supplementary Figure 5A,B**). Next, we explored whether interferon pre-
 168 treatment could potentiate the response of AVI-4206 using SARS-CoV-2 replicons (Taha et al. 2023a) as we
 169 previously demonstrated for a Mac1 deficient SARS-CoV-2 replicon (WA1 N40D mutant) (Alhammad et al.
 170 2023; Taha et al. 2023b) (**Figure 3C**). We did not observe a reduction in viral RNA replication of the Mac1
 171 deficient replicon compared with the wild-type replicon in Vero cells stably expressing ACE2 and TMPRSS2
 172 (VAT) or A549-ACE2^h cells treated with or without AVI-4206 and 1000 IU/ml of IFN-gamma
 173 (**Supplementary Figure 5C,D**). However, there was a modest dose-dependent decrease in replication of the
 174 wild-type, but not Mac1 deficient, replicon in A549-ACE2^h cells (**Supplementary Figure 5D**). When the IFN-
 175 gamma dose was increased to 10000 IU/ml, we observed a small (~1.6-fold) effect for the Mac1 deficient

176 replicon relative to the wild-type replicon (**Figure 3D**). Treatment with highest dose (100 μ M) of AVI-4206 led
177 to a statistically significant, but small (~1.7-fold), reduction in replication for the wild-type, but not Mac1-
178 deficient, replicon (**Figure 3D**). From these experiments, we conclude that cellular models of SARS-CoV-2
179 infection give, at best, only a narrow window for assessing the efficacy of Mac1 inhibition and that high
180 concentrations of AVI-4206 can achieve a limited anti-viral response without cytotoxicity in an IFN- and Mac1
181 catalytic activity-dependent manner.

182
183 To test AVI-4206 in a system that more closely replicates both the structural and functional characteristics of
184 the human airway epithelium, we used human airway organoids (HAOs), which are derived from primary stem
185 cells generated from human lungs and grow as complex three-dimensional structures (Sachs et al. 2019).
186 These cells can be differentiated into the various cell types found in the airway epithelium, including ciliated,
187 goblet, and basal cells (Li et al. 2023a; Simoneau et al. 2024). We (Simoneau et al. 2024) and others (Li et
188 al. 2023a) have utilized differentiated HAOs as a more relevant infection model that encompasses more
189 robust innate immune functions. We therefore sought to test the efficacy of AVI-4206 in HAOs infected with
190 SARS-CoV-2 (**Figure 3E**). The Mac1 deficient virus (WA1 N40D mutant) showed no reduction, 10-fold
191 reduction, and 1000-fold reduction in viral particle production at 24, 48, and 72 hours post-infection compared
192 to the wild-type virus (**Figure 3F**). AVI-4206 treatment reduced viral particle production 10- and 100-fold at
193 48 and 72 hours post-infection, respectively, and 20 μ M AVI-4206 reduced viral particle production by 10-fold
194 at 72 hours post-infection (**Figure 3F**). As we have observed previously (Alhammad et al. 2023; Taha et al.
195 2023b), the faster clearance of infection in AVI-4206 treated HAOs, similar to that seen with the Mac1 deficient
196 virus, is likely due to a potent innate immune response rather than a direct effect of Mac1 on viral replication.
197 While these cellular and organoid experiments gave some indication of an effect of AVI-4206, testing in animal
198 models was required to establish whether this compound had significant activity in reducing viral
199 pathogenesis.

200

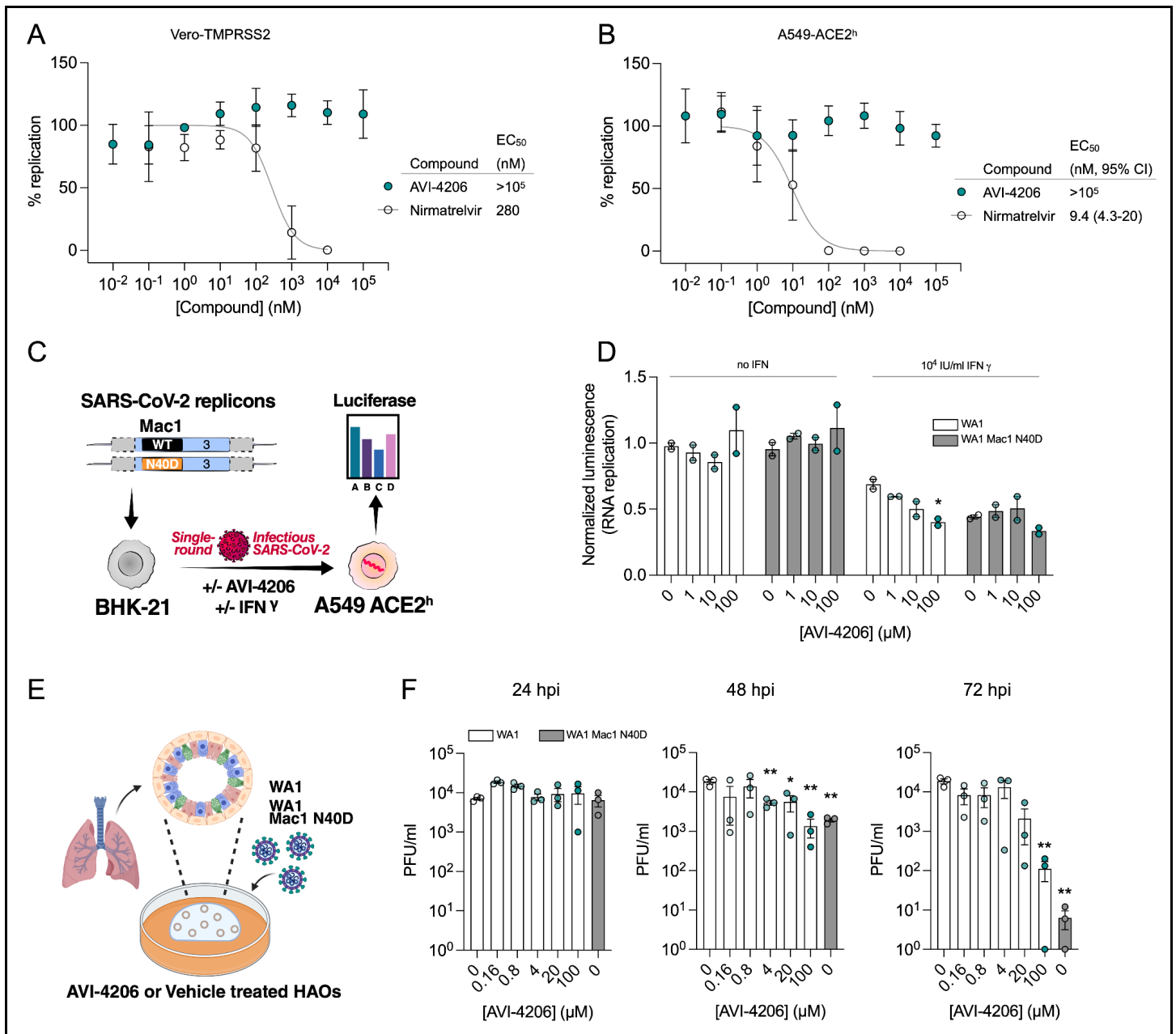


Figure 3: AVI-4206 shows limited efficacy in cellular models of SARS-CoV-2 infection.

(A and B) Vero-TMPRSS2 (A) or A549-ACE2^h (B) cells were pretreated with compounds and infected with mNeonGreen reporter SARS-CoV-2. mNeonGreen expression was measured by the Incucyte system. Graphs represent mean +/- SD of % replication normalized to the DMSO control 24 post-infection of three independent experiments performed in triplicate. Data were fitted with a sigmoidal dose-response equation using non-linear regression (gray line) and the EC₅₀ values are quoted with 95% confidence intervals.

(C) Schematic of the replicon assay to test the efficacy of AVI-4206 in A549 ACE2^h cells.

(D) Luciferase readout of A549 ACE2^h cells infected with WA1 or WA1 Mac1 N40D replicons and treated with or without AVI-4206 and IFN-γ at indicated concentrations; *, *P* < 0.05 by two-tailed Student's t-test relative to the no AVI-4206 and no IFN-γ control. Results are plotted as normalized mean ± standard deviation luciferase values of a representative biological experiment containing two technical replicates.

(E) Schematic of the HAO experiment.

(F) Viral particle production was measured by plaque assay at indicated time points and AVI-4206 concentrations. Error bars indicate s.e.m. **, *P* < 0.01; *, *P* < 0.05 by two-tailed Student's t-test relative to the vehicle control.

202 AVI-4206 has favorable pharmacological properties

203 Prior to testing the efficacy of AVI-4206 in animal models, we assessed the pharmacological properties of the
204 compound to predict a dosing regime that would provide sufficient target coverage to test efficacy. In parallel
205 with optimizing compounds for potent inhibition of Mac1, as described above, we employed data from
206 standard *in vitro* assays of metabolism, permeability, and physicochemical properties to drive our medicinal
207 chemistry campaign. Thus, the series leading to AVI-4206 was optimized for stability in mouse liver
208 microsomes and human hepatocytes, low plasma protein binding (good free fraction), and high aqueous
209 solubility (**Figure 4A**). However, the introduction of the urea functionality in this series negatively impacted
210 permeability in Caco-2 monolayers when compared to the parent AVI-219, predicting low oral bioavailability.
211 Indeed, in mouse pharmacokinetic (PK) studies, AVI-4206 showed poor oral bioavailability (<4%), while
212 intrinsic clearance was moderate, about 60% of hepatic blood flow (**Supplementary Table 3**). Bioavailability
213 via the intraperitoneal (IP) route however, was excellent and free drug concentrations ~100-fold above the
214 biochemical IC₅₀ were achieved for 8 hours following a single IP dose at 100 mg/kg (**Figure 4B**,
215 **Supplementary Table 3**). In a separate PK experiment employing a 10 mg/kg IP dose, total exposure of AVI-
216 4206 in lung was higher than in plasma at later time points, (**Figure 4C**), suggesting its suitability for an *in*
217 *vivo* infection model to validate Mac1 as an antiviral target. Moreover, AVI-4206 showed minimal inhibition of
218 common cytochrome P450 (CYP) isoforms (**Figure 4D**) and a broader panel of potential off targets
219 (**Figure 4E, Supplementary Table 4**), identified no significant liabilities among major channels, receptors, or
220 enzymes. Overall, the biochemical potency and PK profile of AVI-4206 suggested the likelihood of sustained
221 target engagement in mice with twice daily doses (BID) of 100 mg/kg by the IP route allowing us to test proof-
222 of-concept.

223
224

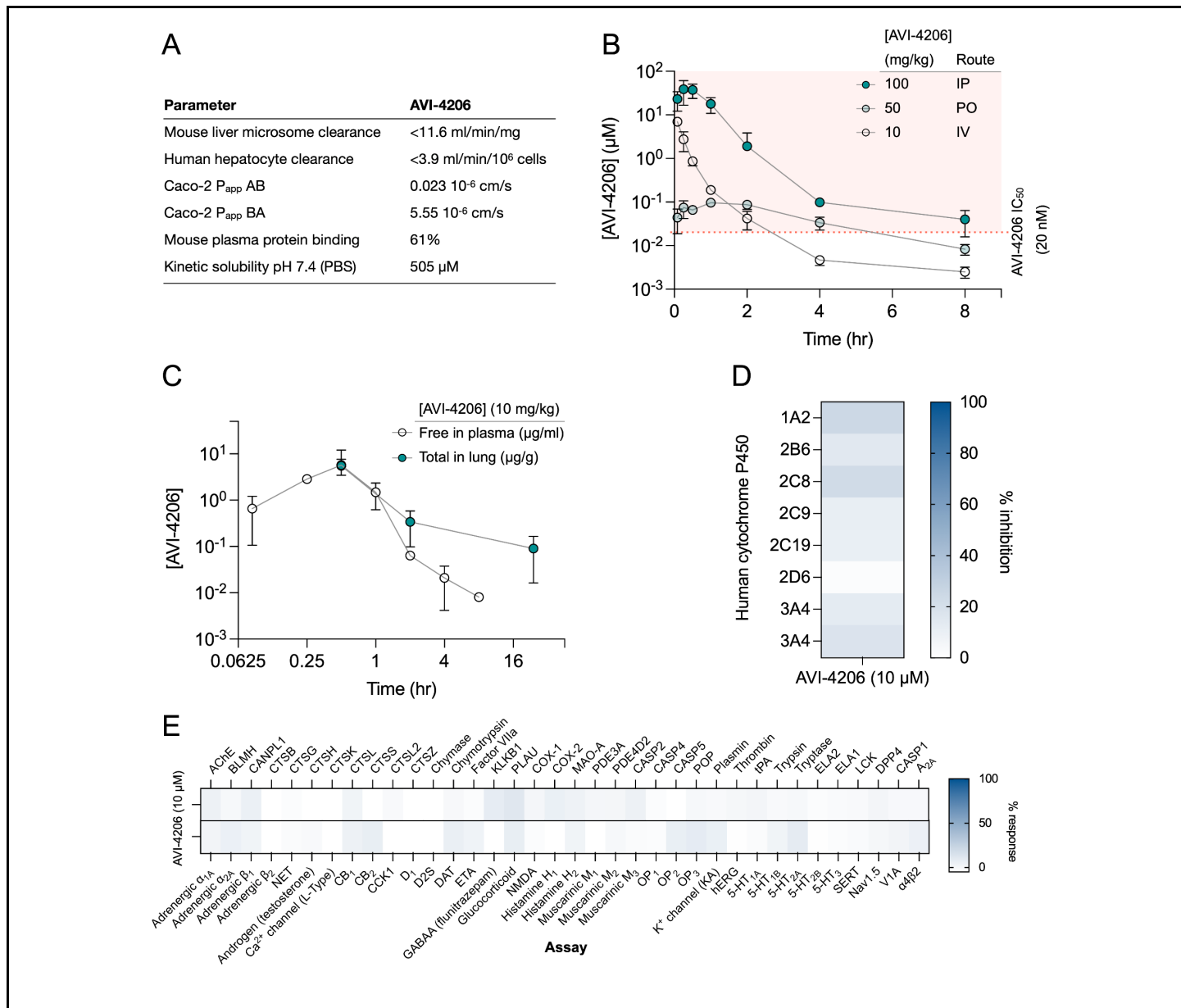


Figure 4: AVI-4206 has a favorable pharmacological profile.

(A) Pharmacokinetic properties of AVI-4206.

(B) Unbound plasma exposure time course of AVI-4206, corrected for plasma protein binding, following administration by IV, PO, or IP routes in male CD-1 mice at the indicated doses.

(C) Free plasma exposure of AVI-4206 and total exposure in lung homogenate following an IP dose of 10 mg/kg in female C57BL/6 mice.

(D) Inhibition of CYP isoforms by AVI-4206 at a fixed concentration of 10 μM. Two experiments were performed with CYP3A4 using different positive controls.

(E) Heatmap of AVI-4206 activity in an off-target safety panel including receptors, ion channels, and proteases, showing no antagonist response >15% at 10 μM.

225

226 AVI-4206 is effective in a mouse model of SARS-CoV-2 infection

227 To assess the efficacy of AVI-4206 *in vivo*, we used the K18-hACE2 mouse model, which mimics severe
 228 SARS-CoV-2 infection (Zheng et al. 2021). The K18-hACE2 mouse is a stringent model to test efficacy, as
 229 previous studies using potent protease inhibitors did not lead to full survival, unless combined with
 230 molnupiravir (Papini et al. 2024). In our experiment, animals were divided into three groups (wild-type WA1

231 virus with compound or vehicle treatment, and a Mac1 deficient mutant-infected positive control) with
232 treatment (AVI-4206 at 100 mg/kg intraperitoneally, nirmatrelvir at 300 mg/kg orally, or vehicle control for each
233 drug) initiated one day prior to infection (**Figure 5A**). AVI-4206 or nirmatrelvir were administered twice daily
234 until 5 days post-infection, during which the mice were closely monitored for disease parameters such as
235 weight loss and hunched posture. Both vehicle-treated groups experienced weight loss starting at 3-4 days
236 post-infection and continued losing weight until the end of the study at 7 days post-infection (**Figure 5B,C**).
237 The AVI-4206 and nirmatrelvir treated groups experienced weight loss starting at 4 days post-infection, but
238 the extent of weight loss was about 5-10% lower on average at days 5-7 post-infection compared with their
239 respective vehicle-treated groups (**Figure 5B,C**). Consequently, ~70% of AVI-4206 treated group and 40% of
240 the nirmatrelvir treated group survived, whereas all mice in the vehicle treated groups died by the end of the
241 study based on the humane endpoints of hunched posture or >20% decrease in body weight (**Figure 5D,E**).
242 Consistent with previous studies (Taha et al. 2023b), none of the mice in the mutant-infected positive control
243 group experienced weight loss, and all survived the infection (**Figure 5D**). These results indicate that AVI-
244 4206 can significantly reduce disease severity and prevent death in the K18-hACE2 model and is comparable
245 to the FDA-approved protease inhibitor nirmatrelvir.

246 To understand the mechanism of AVI-4206 action during the course of infection, mice from each group were
247 euthanized at either day 4 or 7. We observed that AVI-4206 treatment reduced viral load in the lungs by ~10-
248 fold and ~100-fold at 4 and 7 days post-infection, respectively, and reduced transmission to the brain
249 (**Figure 5F**). Although it is possible that AVI-4206 crosses the blood-brain barrier, it is more likely that the
250 reduction of viral load in the brain is as a consequence of a reduction in overall systemic viral load. The
251 prevention of virus localization to the brain is especially important in this model because human ACE2
252 overexpression allows virus replication and spread to brain tissue which ultimately leads to encephalitis and
253 the death of infected mice (Bao et al. 2020; Oladunni et al. 2020). The faster clearance of viral load in the
254 lungs for AVI-4206 treated and Mac1 deficient virus infected mice compared with the vehicle-treated mice,
255 rather than an early antiviral effect post-infection, is consistent with an immune response mediated
256 mechanism rather than a direct antiviral mechanism.

257 To further investigate the antiviral mechanism of AVI-4206, we measured the abundance of the antiviral
258 cytokines IP-10, IL-2, IL-6, and TNF- α in lung tissue at 4 and 7 days post-infection (**Figure 5G**). We found
259 that levels of all of these cytokines were elevated at 4 days post-infection. At 7 days post-infection, the AVI-
260 4206 treated and Mac1 deficient virus infected mice maintained significantly higher levels of IP-10, IL-2, and
261 IL-6 ($P < 0.05$) compared to the vehicle treated group; TNF- α showed a similar trend but did not reach
262 statistical significance (**Figure 5G**). The lower levels of cytokines in the vehicle-treated group at 7 days post-
263 infection is likely mediated by the immune-suppressive capability of SARS-CoV-2 macrodomain. However,
264 when the macrodomain is inactivated, either through AVI-4206 treatment or infection with Mac-1 defective
265 variant, the antiviral response is enhanced, which blocks viral replication. The cumulative cytokine abundance
266 (IP-10, IL-2, and IL-6) indicates an antiviral immune response, likely mediated through the activation of the
267 NF- κ B pathway (Neufeldt et al. 2022; Robertson et al. 2023). Finally, we tested the efficacy of AVI-4206 at a
268 lower dosage of 30 mg/kg using the same experimental setup. Even at this lower dose, AVI-4206 enhanced
269 survival and produced lower viral load at 7 days post-infection relative to vehicle (**Supplementary Figure 6**),
270 but to a more modest degree than at the higher dose (**Figure 5**). Collectively, our observations of enhanced
271 survival of mice, reduced viral load, and an increase in antiviral cytokines suggest that AVI-4206 is capable
272 of potentiating the host immune response, thereby reducing disease severity.

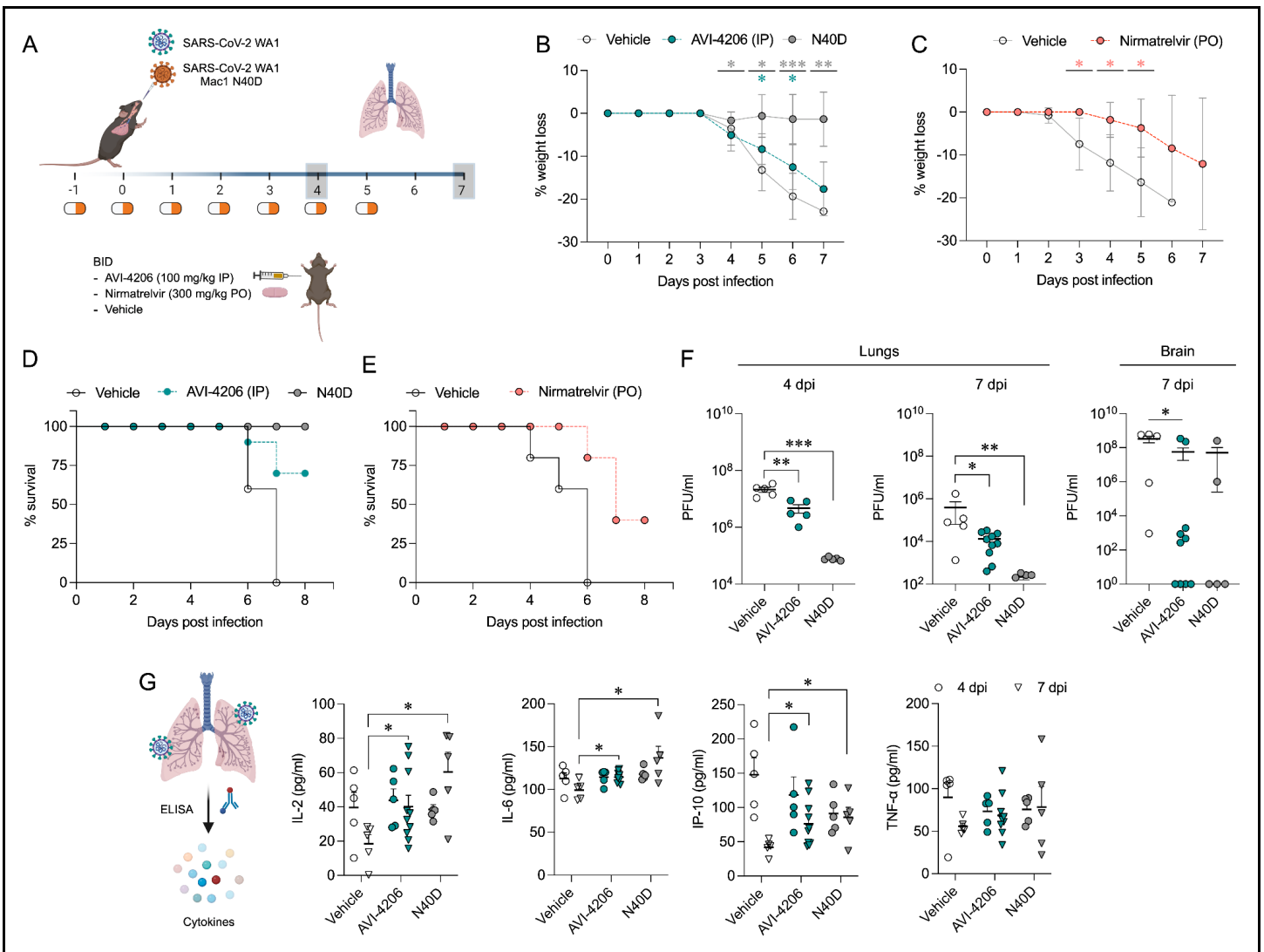


Figure 5: AVI-4206 reduces viral replication and increases survival and cytokine abundance *in vivo*.

(A) K18-hACE2 mice were intranasally infected and dosed as indicated with either AVI-4206 (n=15, intraperitoneally), nirmatrelvir (n=5, per os) or vehicle (n=10 for the AVI-4206 group or n=5 for the nirmatrelvir group). Mice infected with WA1 N40D mutant, which lacks Mac1 catalytic activity, served as a positive control (n=10). Lungs were harvested at indicated time points for virus titration by plaque assay.

(B) The percent body weight loss for all animals treated with AVI-4206 (100 mg/kg IP) (C) or nirmatrelvir (300 mg/kg PO). The data are presented as mean \pm SD. *, $P < 0.05$; **, $P < 0.01$; ***, $P < 0.001$ by two-tailed Student's t-test relative to the vehicle control at each timepoint.

(D) Survival curve plotted based on the percent weight loss humane endpoint (20%) for AVI-4206 and (E) nirmatrelvir.

(F) Viral load in the lungs and brain of infected mice at the indicated time points. The data are shown as mean \pm s.e.m. *, $P < 0.05$; **, $P < 0.01$ by Mann Whitney's test relative to the vehicle control.

(G) Schematics and graphs demonstrating the abundance of indicated cytokines at 4 and 7 days post-infection in the lungs of infected mice. The data are presented as mean \pm s.e.m. *, $P < 0.05$; **, $P < 0.01$ by two-tailed Student's t-test relative to the vehicle control at each timepoint. None of the mice reached the humane endpoint at day 4 post-infection. For mice that reached the humane endpoint before day 7 post-infection, the tissues were collected and analyzed with mice at the 7 day time point.

273

274

Discussion

275

276

277

Here we provide strong pharmacological evidence validating Mac1 and de-ADP-ribosylation as a therapeutic target for SARS-CoV-2. AVI-4206 is a competitive inhibitor that blocks the ADP-ribosylhydrolase activity of Mac1. This activity antagonizes the PARP-mediated ADP-ribosylation that is part of the antiviral interferon

278 response. Although mechanistic links are still emerging between specific post-translational modifications and
279 an effective antiviral response, our pharmacologic studies add to the genetic and biochemical evidence of the
280 importance of this signaling axis for viral replication *in vivo* (Alhammad et al. 2023; Taha et al. 2023b). Our
281 work also adds to the growing role of modulating ADP-ribosylation signaling in therapeutic development
282 (Dasovich and Leung 2023). For example, inhibitors of PARP1, which catalyzes the addition of poly-ADP-
283 ribose marks, have been developed for treating tumors with mutations in either *BRCA1* or *BRCA2* (Lord and
284 Ashworth 2017) and inhibitors of PARG, which catalyzes the removal of $\alpha(1''-2')$ O-glycosidic linkages in PAR
285 chains, are under investigation for a variety of cancers (Slade 2020). The presence of macrodomains and
286 experimental evidence for them as interferon signaling antagonists in other diverse viruses, such as
287 Chikungunya (McPherson et al. 2017), suggests that inhibiting this target class may be effective for treatment
288 of other virally-induced diseases beyond COVID.

289 While AVI-4206 is protective in an animal model of infection, it was developed without many of the normal
290 intermediate markers of improvement in cellular models. This discordance was expected based on the
291 mechanism of action, as interferon-based antiviral activity likely requires intra- and inter-cellular and systemic
292 communication between different cell types (Platanias 2005). The limited replication defect difference
293 between wild-type and Mac1 deficient viruses in cellular models renders them largely ineffective as a model
294 to test the effects of macrodomain inhibition, which has led others to question the validity of Mac1 as target
295 (Lee et al. 2024). AVI-4206 did in fact demonstrate modest antiviral activity only in the presence of exogenous
296 IFN in cells, which is consistent with most other studies that have examined Mac1 activity (Alhammad et al.
297 2023; Taha et al. 2023b; Kerr et al. 2024). While a larger replication defect is observed in HAOs likely due to
298 their more relevant antiviral innate immune responses (Simoneau et al. 2024), the highest dose of AVI-4206
299 does not achieve the magnitude of the replication defect of the Mac1 deficient virus. This may reflect an
300 unoptimized prophylactic dosing schedule or the need to better tune the pharmacological properties of the
301 inhibitor. Taken together, the concordance of *in vitro* (HTRF) and cellular target engagement assays (CETSA)
302 stands out as particularly important in the development path of macrodomain inhibitors.

303 AVI-4206 blocks the viral enzymatic removal of post-translational modifications important for the immune
304 response, which is an important mechanism for blocking virus replication and reducing disease severity.
305 Notably, Mac1 represents a second pharmacologically validated enzymatic domain within Nsp3: a recently
306 developed inhibitor of the papain-like protease (PLpro) domain also shows efficacy in animal models and acts
307 by removing a distinct set of host post-translational modifications (ubiquitin and interferon-stimulated gene 15
308 (ISG15)) (Tan et al. 2024). In summary, AVI-4206 provides proof-of-concept for the validation of a novel
309 antiviral target, Mac1. By restoring the antiviral immune response, the novel mechanism of action of AVI-4206
310 could be synergistic or additive with orthogonally acting direct antivirals, such as protease and polymerase
311 inhibitors, in combination therapies for the treatment of SARS-CoV-2 infection and beyond.

312 Acknowledgments

313 This work was supported by the National Institutes of Health (NIAID Antiviral Drug Discovery (AViDD) grant
314 U19AI171110. M.O. is supported by the James B. Pendleton Charitable Trust and the Roddenberry
315 Foundation. The synchrotron X-ray diffraction data used to determine Mac1 structures were collected at
316 beamline 8.3.1 of the Advanced Light Source (ALS) and beamlines 9-2, 12-1 and 12-2 of the Stanford
317 Synchrotron Radiation Lightsource (SSRL). The ALS, a U.S. DOE Office of Science User Facility under
318 contract no. DE-AC02-05CH11231, is supported in part by the ALS-ENABLE program funded by the NIH,
319 National Institute of General Medical Sciences, grant P30 GM124169. Use of the SSRL, SLAC National
320 Accelerator Laboratory, is supported by the U.S. Department of Energy, Office of Science, Office of Basic
321 Energy Sciences under Contract No. DE-AC02-76SF00515. The SSRL Structural Molecular Biology Program
322 is supported by the DOE Office of Biological and Environmental Research, and by the National Institutes of
323 Health, National Institute of General Medical Sciences (P30GM133894).

324

325

326 Methods

327 Synthetic Chemistry

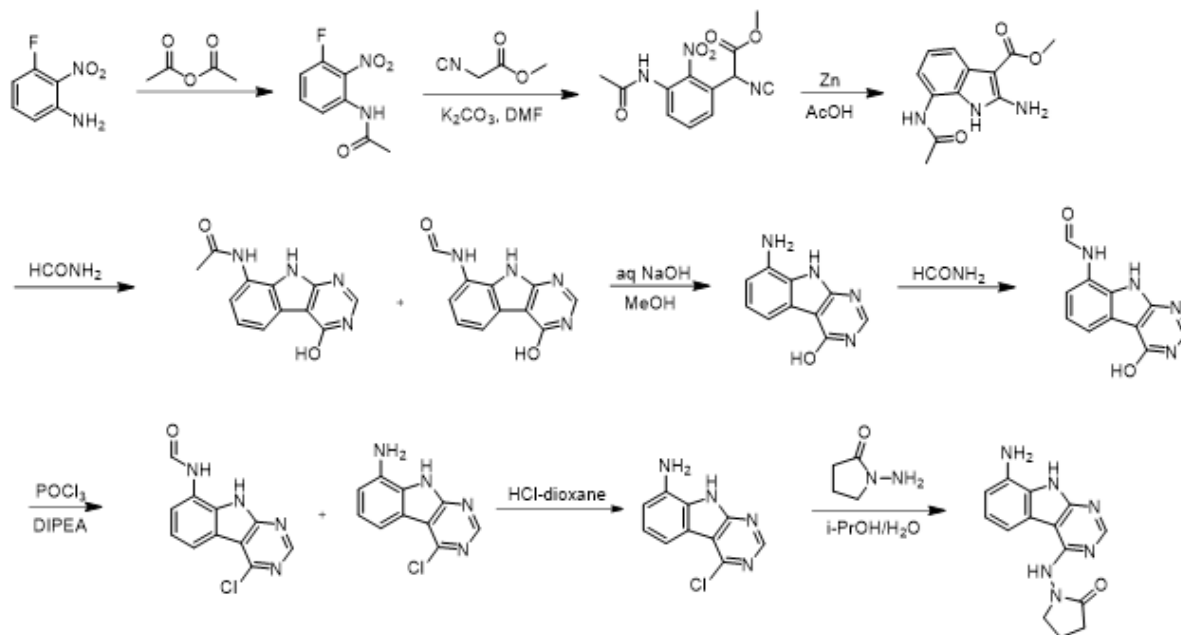
328 **General Experimental Procedures:**

329 Unless otherwise noted all chemical reagents and solvents used are commercially available. AVI-92 and AVI-
330 219 were synthesized as previously described (Gahbauer et al. 2023). Reverse phase chromatography was
331 carried out on one of the following instruments: (i) Waters 2535 Separation module with Waters 2998
332 Photodiode Array Detector. Separations were carried out on XBridge Preparative C18, 19 × 50 mm column
333 at ambient temperature using a mobile phase gradient of water-acetonitrile-0.1% formic acid. (ii) Gilson GX-
334 281 instrument, separations using Xtimate Prep C18, 21.2*250 mm, 150 Å, 10 µm particle size column.(iii)
335 Agilent 1260 Infinity systems equipped with DAD and mass-detector. Separations carried out on Chromatorex
336 18 SMB100-5T 100x19 mm 5 µm column using mobile phase gradient of water/methanol/0.005% HCl. Chiral
337 separations were carried out on CHIRALPAK IA (250x21 mm, 5 µm)-II column at ambient temperature using
338 a mobile phase of hexane (0.3% DEA): IPA:MeOH, 90:5:5. LC/MS data were acquired by one of the following
339 instruments: (i) Waters Acquity UPLC QDa mass spectrometer equipped with Quaternary Solvent Manager,
340 Photodiode Array Detector and Evaporative Light Scattering Detector. Separations were carried out with
341 Acquity UPLC BEH C18 1.7 mm, 2.1 × 50 mm column at 25°C, using a mobile phase gradient of water-
342 acetonitrile containing a constant 0.1% formic acid. Detection: UV (254 nm), ELS and MS (ESI, positive
343 mode), (ii) Agilent 1100 Series LC/MSD system with DAD\ELSD Alltech 2000ES and Agilent LC\MSD VL
344 (G1956B), SL (G1956B) mass-spectrometer, (iii) Agilent 1200 Series LC/MSD system with DAD\ELSD Alltech
345 3300 and Agilent LC\MSD G6130A, G6120B mass-spectrometer, (iv) Agilent Technologies 1260 Infinity
346 LC/MSD system with DAD\ELSD Alltech 3300 and Agilent LC\MSD G6120B mass-spectrometer, or (v)
347 Agilent Technologies 1260 Infinity II LC/MSD system with DAD\ELSD G7102A 1290 Infinity II and Agilent
348 LC\MSD G6120B mass-spectrometer. Separations were carried out with_InfinityLab Poroshell 120 SB-C18
349 4.6x30 mm 2.7 µm column at 25°C, using a mobile phase gradient of water-acetonitrile containing a constant
350 0.1% formic acid. Detection using DAD1A 215 nm, DAD1B 254 nm MSD – single quadrupole, AP-ESI
351 (positive/negative mode switching). (vi) Agilent 1200 Infinity LC with an Agilent 1956 single quadrupole MS
352 using electrospray ionization. Separations were carried out on a SunFire C18 (4.6x 50 mm, 3.5 µm) column
353 at 50°C using a mobile phase gradient of water (10 mmol NH₄HCO₃) / acetonitrile. Detection: UV (214, 254
354 nm) and MS (ESI, POS mode ,103 to 100 atomic mass units). Chemical shifts are reported in units of ppm.
355 NMR spectra were referenced relative to residual NMR solvent peaks. Coupling constants (J) are reported in
356 hertz (Hz). NMR spectra were recorded on one of the following instruments: (i) Bruker AVANCE DRX 500
357 (500 MHz magnet with 5 mm QNP ³¹P/¹³C/¹⁵N and 5 mm TXI probe), (ii) Agilent ProPulse 600 (600 MHz
358 magnet with 5 mm OneNMR probe) and (iii) Bruker Avance III HD 400 MHz spectrometer.

359

360 **1-((8-Amino-9H-pyrimido[4,5-b]indol-4-yl)amino)pyrrolidin-2-one**

361



363 A solution 3-fluoro-2-nitroaniline (11 g, 70.51 mmol) in acetic anhydride (20 ml) was stirred at room
364 temperature for 16 hours. The reaction mixture was filtered and the solids were washed with petroleum ether
365 (100 ml) and dried to obtain 10.7 g (77%) of N-(3-fluoro-2-nitrophenyl)acetamide as a brown solid. LCMS
366 (ESI): $m/z = 199.3$ (M+H)⁺

367 To a solution of N-(3-fluoro-2-nitrophenyl)acetamide (10.7 g, 54.04 mmol) in DMF (100 ml) was added methyl
368 2-isocyanoacetate (8.02 g, 81.06 mmol) and potassium carbonate (14.92 g, 108.08 mmol). After stirring at
369 80°C for 2 hours, the reaction mixture was cooled to room temperature, acidified with 2 N HCl (ca. 2000 ml),
370 and extracted with ethyl acetate (300 ml *3). The combined organic layers were washed with brine (100 ml),
371 dried over sodium sulfate and concentrated under reduced pressure. The residue was purified by silica gel
372 chromatography (10:1 petroleum ether/ethyl acetate) to obtain 11 g (73%) of methyl 2-(3-acetamido-2-
373 nitrophenyl)-2-isocyanoacetate as a yellow solid. LCMS (ESI): $m/z = 278.2$ (M+H)⁺

374 To a solution of methyl 2-(3-acetamido-2-nitrophenyl)-2-isocyanoacetate (11 g, 39.71 mmol) in *glacial* acetic
375 acid (100 ml), was added slowly zinc dust (25.81 g, 397.10 mmol) in two portions. After stirring at 60°C for 2
376 h, the reaction mixture was cooled to room temperature, filtered and washed with THF. The filtrate was
377 concentrated under reduced pressure and purified by silica gel chromatography (10:1
378 dichloromethane/methanol) to obtain 6.2 g (63%) of methyl 7-acetamido-2-amino-1H-indole-3-carboxylate as
379 a yellow solid. LCMS (ESI): $m/z = 248.3$ (M+H)⁺

380 A solution of methyl 7-acetamido-2-amino-1H-indole-3-carboxylate (6.2 g, 25.10 mmol) in formamide (450 ml)
381 was stirred at 220°C for 2 hours. The reaction mixture was then cooled to room temperature and poured in
382 100 ml of water. The resulting mixture was allowed to stand for 15 min before the solids were collected by
383 filtration, washed with water, and dried to obtain 4.1 g of a 1:2 mixture of N-(4-hydroxy-9H-pyrimido[4,5-
384 b]indol-8-yl)acetamide and N-(4-hydroxy-9H-pyrimido[4,5-b]indol-8-yl)formamide. This mixture was taken in
385 methanol (25 ml) and aqueous 12 N NaOH (25 ml). After stirring at 60°C for 16 h, the reaction mixture was
386 then cooled to room temperature, concentrated under reduced pressure to remove methanol and the residue
387 was poured into 100 ml of water. The resulting mixture was allowed to stand for 15 min before the solids were
388 collected by filtration, washed with water, and dried to obtain 3.5 g (70%) of 8-amino-9H-pyrimido[4,5-b]indol-
389 4-ol as a brown solid. LCMS (ESI): $m/z = 201.2$ (M+H)⁺

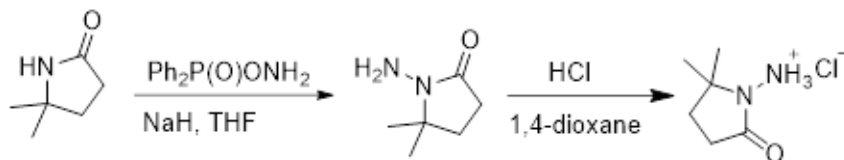
390 A solution of 8-amino-9H-pyrimido[4,5-b]indol-4-ol (3.5g, 17.5 mmol) in formamide (30 ml) was stirred at
391 150°C. After 6 h, the reaction mixture was cooled to room temperature and poured into water (200 ml). The
392 resulting mixture was allowed to stand for 15 min before the solids were collected by filtration, washed with

393 water, and dried to obtain 3.5 g (88%) of N-(4-hydroxy-9H-pyrimido[4,5-b]indol-8-yl)formamide as a brown
394 solid. LCMS (ESI): $m/z = 229.2$ (M+H)⁺

395 To a solution of N-(4-hydroxy-9H-pyrimido[4,5-b]indol-8-yl)formamide (3.5 g, 15.35 mmol) in phosphorous
396 oxychloride (30 ml) was added N,N-diisopropylethylamine (5.94 g, 46.05 mmol), After refluxing for 16 hours,
397 the reaction mixture was cooled to room temperature, concentrated and poured into water (20 ml). The
398 resulting solid was filtered to obtain 500 mg of a mixture of N-(4-chloro-9H-pyrimido[4,5-b]indol-8-
399 yl)formamide and 4-chloro-9H-pyrimido[4,5-b]indol-8-amine as a black solid. This mixture was taken in 4 N
400 HCl in dioxane (15 ml). After stirring at room temperature for 4 h, reaction mixture was concentrated under
401 reduced pressure, the residue was adjusted to pH 7 with aqueous Na₂CO₃, and extracted with ethyl acetate
402 (3 × 30 ml). The organic layers was dried over sodium sulfate, concentrated under reduced pressure and the
403 residue was purified by reverse phase chromatography (water/acetonitrile / 0.1% ammonium bicarbonate) to
404 obtain 320 mg (10%) of 4-chloro-9H-pyrimido[4,5-b]indol-8-amine as a white solid. ¹H NMR (500 MHz, DMSO)
405 δ 12.42 (s, 1H), 8.74 (s, 1H), 7.58 (d, *J* = 7.8 Hz, 1H), 7.25–7.08 (m, 1H), 6.93 (d, *J* = 7.7 Hz, 1H), 5.76 (s,
406 2H). LCMS (ESI): $m/z = 219.2$ (M+H)⁺

407 A mixture of 4-chloro-9H-pyrimido[4,5-b]indol-8-amine (28 mg, 0.13 mmol) and 1-aminopyrrolidin-2-one
408 hydrochloride (35 mg, 0.26 mmol) in isopropanol/water (10: 1, 1.1 ml) were heated to 100°C for 18 h. The
409 reaction mixture was filtered, the residue was washed with ethyl acetate and dried to obtain 28 mg (77%) of
410 1-((8-amino-9H-pyrimido[4,5-b]indol-4-yl)amino)pyrrolidin-2-one as brown solid. ¹H NMR (DMSO-d₆, 400
411 MHz) δ 12.99 (br s, 1H), 8.62 (s, 1H), 7.92 (br d, 1H, *J* = 7.5 Hz), 7.27 (t, 1H, *J* = 7.9 Hz), 7.05 (br d, 1H, *J* =
412 7.5 Hz), 3.70 (br t, 2H, *J* = 6.9 Hz), 2.44-2.53 (m, 2H), 2.20 (br t, 2H, *J* = 7.4 Hz). ¹³C NMR (METHANOL-d₄,
413 100 MHz) δ 175.9, 155.9, 154.3, 153.2, 132.5, 125.7, 121.9, 119.4, 111.3, 111.1, 97.0, 48.6, 47.9, 28.5, 15.9.
414 LCMS (ESI): $m/z = 283$ (M+H)⁺

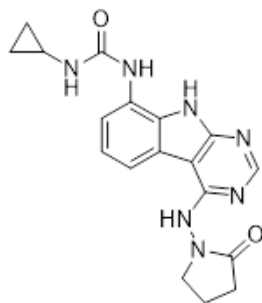
415 **1-Amino-5,5-dimethylpyrrolidin-2-one hydrochloride**



417 To a cooled (0°C) solution of 5,5-dimethylpyrrolidin-2-one (3 g, 26.54 mmol) in THF (60 ml) was added sodium
418 hydride (2.13 g, 53.09 mmol), followed by addition of (aminoxy)diphenylphosphine oxide (12.4 g, 53.09
419 mmol) after 30 min. After stirring the resultant white suspension at 0°C for 2 h, the reaction mixture was filtered
420 through a Celite pad, the filtrate was concentrated and purified by silica gel chromatography (10:1
421 dichloromethane/methanol) to afford 3 g (75%) of 1-amino-5,5-dimethylpyrrolidin-2-one as yellow oil. LCMS
422 (ESI): $m/z = 129.1$ (M+18)⁺;

423 A solution of 1-amino-5,5-dimethylpyrrolidin-2-one (1.5 g, crude) in 4 N HCl in dioxane (15 ml) was stirred at
424 room temperature for 4h. The mixture was concentrated under reduced pressure, residue was triturated with
425 diethyl ether and filtered to afford 1 g (53%) of 1-amino-5,5-dimethylpyrrolidin-2-one hydrochloride salt as a
426 white solid. ¹H NMR (500 MHz, DMSO) δ 9.48 (s, 3H), 2.39 (t, 2H, *J* = 7.8 Hz), 1.90 (t, 2H, *J* = 7.8 Hz), 1.30
427 (s, 6H). LCMS (ESI): $m/z = 129.1$ (M+18)⁺

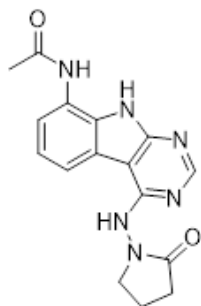
428 **AVI-4051**



429

430 To a solution of 1-((8-amino-9H-pyrimido[4,5-b]indol-4-yl)amino)pyrrolidin-2-one (20 mg, 0.071 mmol) and
431 triethylamine (0.040 ml, 0.28 mmol) in THF (1 ml), was added cyclopropyl isocyanate (24 mg, 0.28 mmol).
432 After stirring at 65 °C for 48 h, the reaction mixture was purified by reverse phase chromatography
433 (water/acetonitrile/0.1% formic acid) to obtain 12 mg (41%) of 1-cyclopropyl-3-(4-((2-oxopyrrolidin-1-
434 yl)amino)-9H-pyrimido[4,5-b]indol-8-yl)urea formic acid salt (AVI-4051) as a white solid. ¹H NMR (DMSO-d₆,
435 400 MHz) δ 11.81 (br s, 1H), 9.31 (s, 1H), 8.50 (br s, 1H), 8.41 (s, 1H), 7.99 (d, 1H, *J* = 7.8 Hz), 7.63 (d, 1H,
436 *J* = 7.8 Hz), 7.21 (t, 1H, *J* = 7.9 Hz), 6.74 (br s, 1H), 3.70 (br t, 2H, *J* = 7.1 Hz), 3.12-3.17 (m, 2H), 2.54-2.65
437 (m, 1H), 2.39-2.43 (m, 2H), 0.98 (t, 2H, *J* = 7.1 Hz), 0.68-0.70 (m, 2H). LCMS (ESI): *m/z* = 366 (M+H)⁺

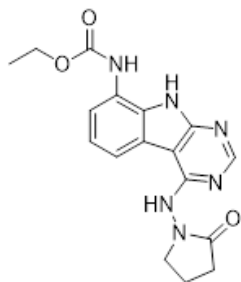
438 AVI-1501



439

440 To a solution of 1-((8-amino-9H-pyrimido[4,5-b]indol-4-yl)amino)pyrrolidin-2-one (15 mg, 0.053 mmol) and
441 triethylamine (0.015 ml, 0.11 mmol) in THF (1 ml), was added acetyl chloride (0.004 ml, 0.056 mmol). After
442 stirring at 65°C for 3 h, the reaction mixture was purified by reverse phase chromatography
443 (water/acetonitrile/0.1% formic acid) to obtain 9 mg (50%) of N-(4-((2-oxopyrrolidin-1-yl)amino)-9H-
444 pyrimido[4,5-b]indol-8-yl)acetamide formic acid (AVI-1501) as a white solid. ¹H NMR (METHANOL-d₄, 400
445 MHz) δ 8.39 (s, 1H), 7.90 (d, 1H, *J* = 7.8 Hz), 7.45 (d, 1H, *J* = 7.8 Hz), 7.19-7.21 (m, 1H), 3.81-3.85 (m, 2H),
446 2.59-2.63 (m, 2H), 2.27-2.31 (m, 5H). LCMS (ESI): *m/z* = 325 (M+H)⁺

447 AVI-3367

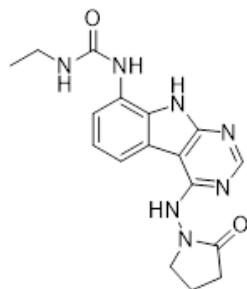


448

449 To a solution of 1-((8-amino-9H-pyrimido[4,5-b]indol-4-yl)amino)pyrrolidin-2-one (15 mg, 0.053 mmol) and
450 triethylamine (0.015 ml, 0.11 mmol) in THF (1 ml), was added ethyl chloroformate (0.005 ml, 0.056 mmol).
451 After stirring at 65°C for 18 h, the reaction mixture was purified by reverse phase chromatography
452 (water/acetonitrile/0.1% formic acid) to obtain 2.7 mg (13%) of ethyl (4-((2-oxopyrrolidin-1-yl)amino)-9H-

453 pyrimido[4,5-b]indol-8-yl)carbamate formic acid salt (**AVI-3367**) as tan solid. ¹H NMR (METHANOL-d₄, 400
454 MHz) δ 8.42 (s, 1H), 7.94 (d, 1H, J = 7.8 Hz), 7.59 (br s, 1H), 7.28 (t, 1H, J = 7.9 Hz), 4.1-4.26-4.30 (m, 2H),
455 3.84 (t, 2H, J = 7.1 Hz), 2.60 (t, 2H, J = 8.0 Hz), 2.30-2.33 (m, 2H), 1.36-1.39 (m, 3H). LCMS (ESI): m/z= 355
456 (M+H)⁺

457 **AVI-1500**

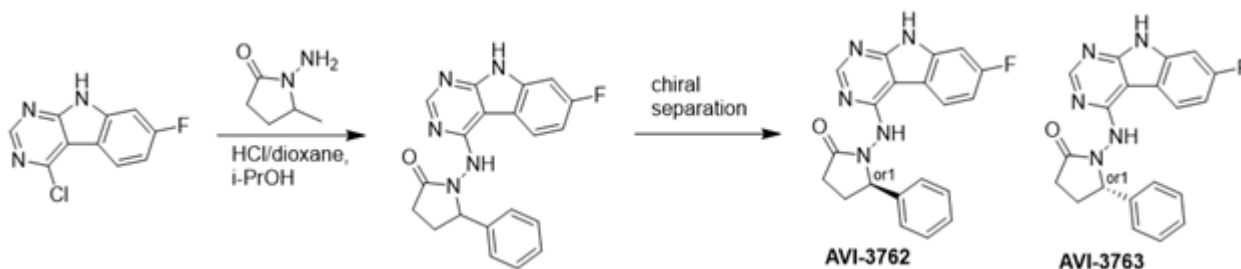


458

459 To a solution of 4-chloro-9H-pyrimido[4,5-b]indol-8-amine (50 mg, 0.23 mmol) and triethylamine (0.064 ml,
460 0.46 mmol) in THF (2 ml), was added ethyl isocyanate (0.018 ml, 0.23 mmol). After stirring at 65°C for 18 h,
461 the reaction mixture was filtered. The residue was washed with ethyl acetate and dried to obtain 50 mg of 1-
462 (4-chloro-9H-pyrimido[4,5-b]indol-8-yl)-3-ethylurea as a white solid that was used without further purification.
463 ¹H NMR (DMSO-d₆, 400 MHz) δ 12.39 (br s, 1H), 8.80 (s, 1H), 8.43 (s, 1H), 7.96 (d, 1H, J = 7.6 Hz), 7.72 (d,
464 1H, J = 7.8 Hz), 7.35 (t, 1H, J = 7.9 Hz), 6.38 (s, 1H), 3.18-3.21 (m, 2H), 1.12 (t, 3H, J = 7.2 Hz). LCMS (ESI):
465 m/z = 290, 292 (M+H)⁺

466 A mixture of 1-(4-chloro-9H-pyrimido[4,5-b]indol-8-yl)-3-ethylurea (26 mg, 0.09 mmol) and 1-aminopyrrolidin-
467 2-one hydrochloride (25 mg, 0.18 mmol) in isopropanol/water (10: 1, 1.1 ml) were heated to 100°C for 18 h.
468 The reaction mixture was purified by reverse phase chromatography (water/acetonitrile/0.1% formic acid) to
469 obtain 8 mg (20%) of 1-ethyl-3-(4-((2-oxopyrrolidin-1-yl)amino)-9H-pyrimido[4,5-b]indol-8-yl)urea formic acid
470 salt (**AVI-1500**) as a white solid. ¹H NMR (DMSO-d₆, 400 MHz) δ 11.75 (br s, 1H), 9.31 (s, 1H), 8.53 (s, 1H),
471 8.41 (s, 1H), 7.97 (d, 1H, J = 7.8 Hz), 7.63 (d, 1H, J = 7.8 Hz), 7.20 (t, 2H, J = 7.9 Hz), 6.37 (br s, 1H), 3.70
472 (t, 2H, J = 7.1 Hz), 3.17-3.20 (m, 2H), 2.39-2.41 (m, 2H), 2.12-2.16 (m, 2H), 1.09-1.13 (m, 3H). ¹³C NMR
473 (DMSO-d₆, 100 MHz) δ 173.5, 156.2, 155.9, 155.5, 155.0, 128.5, 125.5, 121.3, 120.3, 117.1, 116.7, 96.4,
474 48.4, 34.8, 28.9, 16.7, 15.9. LCMS (ESI): m/z = 354 (M+H)⁺

475 **AVI-3762 & AVI-3763**



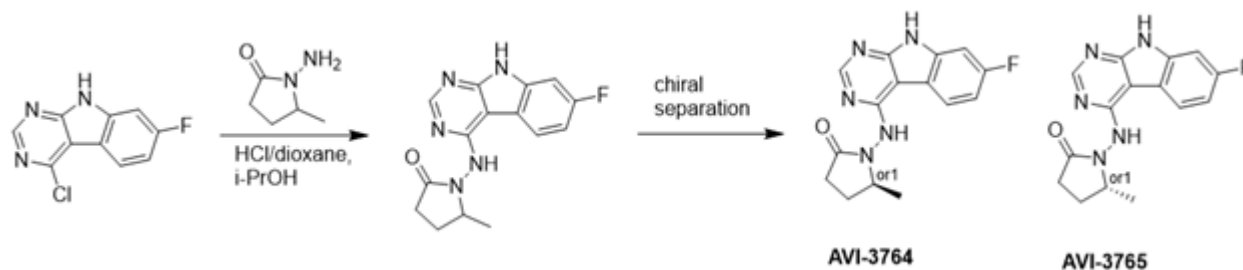
476

477 4-Chloro-7-fluoro-9H-pyrimido[4,5-b]indole (123 mg, 0.55 mmol) and 1-amino-5-phenylpyrrolidin-2-one (117
478 mg, 0.66 mmol) in a mixture of dioxane*HCl/IPA (1.5 ml/1.5 ml) was stirred at 95°C overnight. Upon
479 completion the mixture was cooled to rt and concentrated under reduced pressure. The crude material was
480 purified by HPLC (30-80% MeOH/H₂O) to afford 1-((7-fluoro-9H-pyrimido[4,5-b]indol-4-yl)amino)-5-
481 phenylpyrrolidin-2-one (69 mg, HCl salt, 34% yield). It was further separated by chiral chromatography
482 (Hexane-IPA-MeOH, 50-25-25) to obtain **AVI-3762** (27 mg, retention time = 14.04 min, 99% opt ee) and
483 **AVI-3763** (26 mg, retention time = 11.17 min, 100% opt ee).

484 **AVI-3762:** H1 NMR (500 MHz,DMSO) δ 12.2 (s, 1H), 9.47-9.28 (m, 1H), 8.41 (s, 1H), 8.24 (dd, J = 8.8, 5.5
485 Hz, 1H), 7.45 (d, J = 7.1 Hz, 1H), 7.32 (t, J = 7.4 Hz, 1H), 7.27-7.18 (m, 1H), 7.14-7 (m, 1H), 5.26-5.07 (m,
486 1H), 2.57-2.49 (m, 3H), 1.93-1.78 (m, 1H). LCMS (ESI): m/z = 362 (M+H)+

487 **AVI-3763:** H1 NMR (500 MHz,DMSO) δ 12.2 (s, 1H), 9.5-9.28 (m, 1H), 8.41 (s, 1H), 8.24 (dd, J = 8.5, 5.2 Hz,
488 1H), 7.45 (d, J = 7.1 Hz, 1H), 7.32 (t, J = 7.4 Hz, 1H), 7.28-7.17 (m, 1H), 7.14-7.03 (m, 1H), 5.28-5.06 (m,
489 1H), 2.57-2.49 (m, 3H), 1.97-1.78 (m, 1H). LCMS (ESI): m/z = 362 (M+H)+

490 **AVI-3764 & AVI-3765**

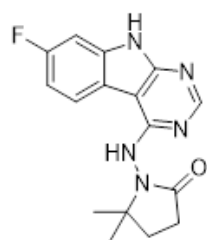


492 4-Chloro-7-fluoro-9H-pyrimido[4,5-b]indole (222 mg, 1.0 mmol) and 1-amino-5-methyl-pyrrolidin-2-one (196
493 mg, 1.3 mmol) in a mixture of dioxane*HCl/IPA (1.5 ml/1.5 ml) was stirred at 95°C overnight. Upon completion
494 the mixture was cooled to rt and concentrated under reduced pressure. The crude material was purified by
495 HPLC (40-90% H₂O/MeOH/0.005% HCl) to afford 1-((7-fluoro-9H-pyrimido[4,5-b]indol-4-yl)amino)-5-
496 methylpyrrolidin-2-one (HCl salt, 0.155 g, 46% yield). It was further subjected chiral chromatography (hexane
497 (0.3% DEA): IPA:MeOH, 90:5:5) to obtain **AVI-3765** (39 mg, retention time = 46.18min, 99% optic ee) and
498 **AVI-3764** (36 mg, retention time = 51.98 min, 90% optic ee).

499 **AVI-3765:** H1 NMR (500 MHz,DMSO) δ 12.22 (s, 1H), 9.31 (s, 1H), 8.47-8.3 (m, 2H), 7.25 (dd, J = 9.6, 1.9
500 Hz, 1H), 7.18-7.11 (m, 1H), 4.03 (s, 1H), 2.39-2.26 (m, 3H), 1.7-1.63 (m, 1H), 1.21 (d, J = 6 Hz, 3H). LCMS
501 (ESI): m/z = 300 (M+H)+

502 **AVI-3764:** H1 NMR (500 MHz,DMSO) δ 12.22 (s, 1H), 9.31 (s, 1H), 8.45-8.37 (m, 1H), 8.35 (s, 1H), 7.25 (dd,
503 J = 9.4, 2.3 Hz, 1H), 7.2-7.04 (m, 1H), 4.11-3.93 (m, 1H), 2.42-2.19 (m, 3H), 1.75-1.57 (m, 1H), 1.21 (d, J
504 = 6.3 Hz, 3H). LCMS (ESI): m/z = 300 (M+H)+

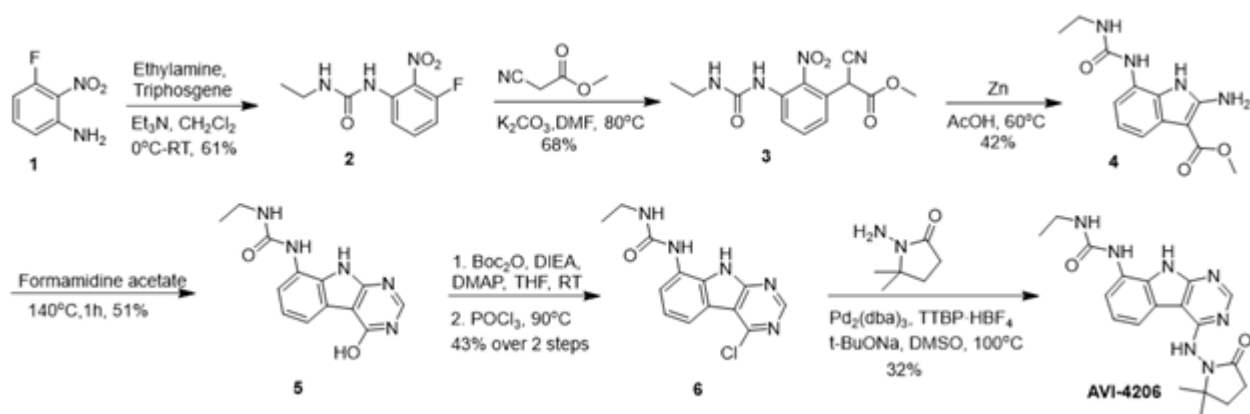
505 **AVI-4636**



506

507 A mixture of 4-chloro-7-fluoro-9H-pyrimido[4,5-b]indole (25 mg, 0.11 mmol) and 1-amino-5,5-
508 dimethylpyrrolidin-2-one hydrochloride salt (28 mg, 0.17 mmol) in isopropanol/aqueous 1N HCl (2: 1, 0.6 ml)
509 were heated to 100°C for 18 h. The reaction mixture was purified by reverse phase chromatography
510 (water/acetonitrile/0.1% formic acid) to obtain 10 mg (25%) of 1-((7-fluoro-9H-pyrimido[4,5-b]indol-4-
511 yl)amino)-5,5-dimethylpyrrolidin-2-one formic acid salt (**AVI-4636**) as a white solid. 1H NMR (METHANOL-
512 d₄, 400 MHz) δ 8.30 (s, 1H), 8.09 (dd, 1H, J = 5.1, 8.8 Hz), 7.21 (dd, 1H, J = 2.3, 9.4 Hz), 6.97 (t, 1H, J = 9.2
513 Hz), 2.59-2.63 (m, 2H), 2.20 (br s, 2H), 1.38 (s, 6H). LCMS (ESI): m/z = 314 (M+H)+

514 **AVI-4206**



515

516 A solution of 3-fluoro-2-nitroaniline (25.00 g, 160 mmol) in THF (500 ml) were added triethylamine (48 g, 480
517 mmol) and triphosgene (14.2 g, 48 mmol) at 0°C. After stirring for an hour, ethylamine as 2.0 M solution in
518 THF (200 ml) was added. Upon completion of reaction, the mixture was poured into 500 ml of water, extracted
519 with ethyl acetate (3 × 500 ml), the combined organic layers were washed with brine (500 ml), dried over
520 sodium sulfate, filtered, concentrated under reduced pressure and the residue was purified by silica gel
521 column chromatography (0–20% ethyl acetate/hexanes) to afford 1-ethyl-3-(3-fluoro-2-nitrophenyl)urea as
522 yellow solid (22.00 g, yield: 60.57%). LCMS (ESI): m/z = 228.1 (M+H)+

523 To a solution of 1-ethyl-3-(3-fluoro-2-nitrophenyl)urea (48 g, 211.45 mmol) in DMF (300 ml) were added
524 methyl 2-isocyanoacetate (41.86 g, 422.90 mmol) and potassium carbonate (87.54 g, 634.36 mmol). The
525 solution was stirred at 80°C for 16 hours. The mixture was adjusted to be weakly acidic by 2N HCl, extracted
526 with ethyl acetate (500 ml *3), the combined organic layers were washed with brine (300 ml), dried over
527 sodium sulfate, filtered and concentrated under reduced pressure, the residue was purified via column
528 chromatography on silica gel (0–20% ethyl acetate/hexanes) to afford methyl 2-cyano-2-(3-(3-ethylureido)-2-
529 nitrophenyl)acetate as yellow solid (44.3 g, yield: 68.46%). LCMS (ESI): m/z = 307.2 (M+H)+.

530 A mixture of methyl 2-cyano-2-(3-(3-ethylureido)-2-nitrophenyl)acetate (42 g, 137.25 mmol) and acetic acid
531 (250 ml) was heated to 40°C. Zinc (89.75 g, 1372.54 mmol) was then added in portions at a rate such that
532 the reaction temperature did not rise above 60°C. After the addition was complete, the reaction mixture was
533 stirred at 60°C for 2 h. The reaction mixture was cooled to room temperature and filtered through a celite pad.
534 The filtrate was concentrated under vacuum. The crude product was purified via column chromatography on
535 silica gel (DCM: MeOH=10:1) to give methyl 2-amino-7-(3-(3-ethylureido)-1H-indole-3-carboxylate) as a white
536 solid (16 g, yield: 42.23%). LCMS (ESI): m/z = 277.2 (M+H)+

537 Methyl 2-amino-7-(3-(3-ethylureido)-1H-indole-3-carboxylate) (2.0 g, 7.25 mmol) and formamidine acetate (4.53
538 g, 43.48 mmol) were heated to 140°C for 1 h. The mixture was cooled to room temperature and diluted with
539 approximately 100 ml of water. The resulting mixture was stirred for 15 min before the solid was collected by
540 filtration. The residue was triturated with DMSO and filtered to afford 1-ethyl-3-(4-hydroxy-9H-pyrimido[4,5-
541 b]indol-8-yl)urea as an off-white solid (1.0 g, yield: 50.8%). ¹H NMR (500 MHz, DMSO) δ 12.21 (s, 1H), 11.76
542 (s, 1H), 8.34 (s, 1H), 8.13 (d, J = 3.5 Hz, 1H), 7.64 (d, J = 7.7 Hz, 1H), 7.40 (d, J = 7.3 Hz, 1H), 7.13 (t, J =
543 7.8 Hz, 1H), 6.28 (t, J = 5.5 Hz, 1H), 3.26–3.11 (m, 2H), 1.10 (t, J = 7.2 Hz, 3H). LCMS (ESI): m/z = 272.3
544 (M+H)+

545 To a solution of 1-ethyl-3-(4-hydroxy-9H-pyrimido[4,5-b]indol-8-yl)urea (500 mg, 1.85 mmol) in THF (20 ml)
546 was added di-*tert*-butyl dicarbonate (1.21 g, 5.54 mmol), DIPEA (955 mg, 7.4 mmol) and DMAP (226 mg,
547 1.85 mmol). The mixture was stirred at room temperature for 16 hours. The mixture was then concentrated
548 under reduced pressure to give crude *tert*-butyl 4-((*tert*-butoxycarbonyl)oxy)-8-(3-(3-ethylureido)-9H-
549 pyrimido[4,5-b]indole-9-carboxylate) as a yellow oil. It was used in the next step without any purification.

550 A solution of *tert*-butyl 4-((*tert*-butoxycarbonyl)oxy)-8-(3-(3-ethylureido)-9H-pyrimido[4,5-b]indole-9-carboxylate
551 (crude) in POCl₃ (10 ml) was stirred at 90°C for 30 min. The solution was concentrated under reduced

552 pressure and diluted with acetonitrile, then adjusted the pH to 7.0 with ammonium hydroxide slowly. The
553 resulting solid was filtered with vacuum filter and washed with water to give the 1-(4-chloro-9H-pyrimido[4,5-
554 b]indol-8-yl)-3-ethylurea (230 mg, two steps yield: 43.1%) as a light yellow solid. LCMS (ESI): m/z = 290.2
555 (M+H)⁺

556 To a solution of 1-(4-chloro-9H-pyrimido[4,5-b]indol-8-yl)-3-ethylurea (290 mg, 1.0 mmol) in dry DMSO (6.0 ml)
557 was added 1-amino-5,5-dimethylpyrrolidin-2-one (192 mg, 1.5 mmol), Pd₂(dba)₃ (92 mg, 0.1 mmol), Tri-tert-
558 butylphosphine tetrafluoroborate (44 mg, 0.15 mmol) and t-BuONa (240 mg, 2.5 mmol). After stirring at 100°C
559 for 8h, the reaction mixture was filtered and the filtrate was purified by reversed phase chromatography (water
560 /acetonitrile/0.1% TFA). After lyophilization, then silica gel column chromatography (DCM/MeOH=10/1) to
561 obtain 1-(4-((2,2-dimethyl-5-oxopyrrolidin-1-yl)amino)-9H-pyrimido[4,5-b]indol-8-yl)-3-ethylurea (**AVI-4206**)
562 (120 mg, yield: 31.5%) as a white solid. ¹H NMR (400 MHz, DMSO) δ 11.67 (s, 1H), 9.06 (s, 1H), 8.37 (d, J =
563 15.7 Hz, 2H), 8.07 (d, J = 7.6 Hz, 1H), 7.59 (d, J = 7.8 Hz, 1H), 7.20 (t, J = 7.9 Hz, 1H), 6.28 (t, J = 5.4 Hz,
564 1H), 3.27–3.10 (m, 2H), 2.42 (t, J = 7.8 Hz, 2H), 2.03 (t, J = 7.8 Hz, 2H), 1.26 (d, J = 21.1 Hz, 6H), 1.11 (t, J
565 = 7.2 Hz, 3H). ¹³C NMR (DMSO-d₆, 100 MHz) δ 171.8, 157.8, 155.9, 155.8, 154.9, 128.6, 125.4, 125.3, 121.2,
566 120.4, 117.2, 117.1, 96.6, 61.1, 34.8, 34.7, 32.4, 27.8, 26.6, 15.9. LCMS (ESI): m/z = 382 (M+H)⁺

567 *In vitro* validation

568 X-ray Crystallography:

569 Mac1 crystals (P4₃ construct, residues 3–169) were grown by sitting-drop vapor diffusion in 28% w/v
570 polyethylene glycol (PEG) 3000 and 100 mM N-cyclohexyl-2-aminoethanesulfonic acid (CHES) pH 9.5 as
571 described previously (Schuller et al. 2021; Gahbauer et al. 2023). Compounds prepared in DMSO (100 mM)
572 were added to crystal drops using an Echo 650 acoustic dispenser (Collins et al. 2017) (final concentration of
573 10 mM). Crystals were incubated at room temperature for 2–4 hours prior to vitrification in liquid nitrogen
574 without additional cryoprotection. X-ray diffraction data were collected at the Advanced Light Source (ALS
575 beamline 8.3.1) or the Stanford Synchrotron Light Source (SSRL beamline 9-2). Data were indexed,
576 integrated and scaled with XDS (Kabsch 2010) and merged with Aimless (Evans and Murshudov 2013). The
577 P4₃ Mac1 crystals contain two copies of the protein in the asymmetric unit (chains A and B). The active site
578 of chain A is open, however chain B is blocked by a crystal contact. We previously observed that potent Mac1
579 inhibitors dissolve crystals, likely through the displacement of the B chain crystal contact (Gahbauer et al.
580 2023). In addition, crystal packing in the chain A active site restricts movement of the Ala129-Gly134 loop,
581 leading to decreased occupancy for compounds with substituents on the pyrrolidinone. To aid modeling the
582 resulting conformational and compositional disorder, we used the PanDDA method (Pearce et al. 2017) to
583 model ligands where the occupancy was low (<25%, AVI-4051, AVI-3367, AVI-3763, AVI-3762, AVI-3765
584 and AVI-3764) or where there was substantial disorder (AVI-4636). After modeling ligands, structures were
585 refined using phenix.refine (Liebschner et al. 2019) as described previously (Gahbauer et al. 2023). Data
586 collection settings and statistics are reported in **Supplementary Table 1**.

587

588 To achieve higher ligand occupancy for AVI-4206, we co-crystallized an alternative Mac1 construct previously
589 reported to crystallize in P1, P2₁ and C2 (residues 2–170) (Michalska et al. 2020; Correy et al. 2022). Crystals
590 grew by sitting-drop vapor diffusion in 200 mM lithium acetate and 20% w/v PEG 3350 with 30 mg/ml Mac1
591 (1.6 mM) and 3.2 mM AVI-4206 (3.2% DMSO). Crystals were vitrified directly in liquid nitrogen and diffraction
592 data to 0.8 Å were collected at the ALS (beamline 8.3.1). Data were reduced in P1 using the same pipeline
593 as the P4₃ crystals. Solvent content analysis suggested that there were two chains in the asymmetric unit.
594 Phases were obtained using Phaser (McCoy et al. 2007) and apo Mac1 coordinates (PDB code 7KQO, chain
595 A). Structural refinement was performed with phenix.refine following the previously described procedures
596 for ultra-high resolution data (Correy et al. 2022). After several rounds of refinement, positive difference
597 density was clear for a second, relatively low occupancy, conformation of the entire chain A and B, each
598 representing a ~3.1 Å translation relative to the major conformation. Modeling and inspection of the minor
599 conformations suggested that they cannot be occupied simultaneously, therefore they were modeled with
600 distinct alternative location identifiers (altlocs). The major conformation (protein, AVI-4206 and water) was
601 modeled with altloc A and the minor conformations (protein, AVI-4206 and water) were modeled with altlocs

602 C and D. In addition to the rigid body disorder, there was clear density for a third conformation of the residue
603 57-75 α -helix. In chain A, this was modeled with altloc B, while the density in chain B was too weak to allow
604 modeling. The $F_o - F_c$ difference electron density maps or PanDDA event maps used to model ligands are
605 shown in **Supplementary Figure 1**.

606

607 **Inhibition assay:**

608 Inhibition of Mac1 ADP-ribosylhydrolase activity by AVI-219 and AVI-4206 was determined using the
609 NUDT5/AMP-Glo assay (Dasovich et al. 2021; Taha et al. 2023b). The substrate for the reaction was human
610 PARP10 (catalytic domain, residues 819-1007), purified and auto-mono-ADP-ribosylated using NAD⁺ as
611 described previously (Taha et al. 2023b). Briefly, AVI-219 and AVI-4206 were dispensed into 384-well white
612 assay plates (Corning, 3824) using an Echo 650 acoustic dispenser to achieve a final concentration range
613 from 1 mM to 0.4 nM (8 μ l reaction volume, 1% DMSO). Purified Mac1 (P4₃ construct, 2 μ l, 10 nM final
614 concentration) and NUDT5 (2 μ l, 100 nM final concentration) were added to wells and the plates were
615 incubated for five minutes at room temperature. Mono-ADP-ribosylated PARP10 was added to wells (4 μ l, 2
616 μ M final concentration) and the plates were incubated at room temperature for an additional hour. The
617 concentration of AMP was measured with an AMP-Glo assay kit (Promega, V5011) following the
618 manufacturer's instructions using a BioTek Synergy HTX plate reader. Percentage inhibition was calculated
619 relative to control wells containing no inhibitor (DMSO only, 0% inhibition) or no Mac1 (100% inhibition) and
620 IC₅₀ values were determined by fitting a four-parameter sigmoidal dose-response equation using GraphPad
621 Prism (version 10.1.1), with the top and bottom constrained to 100 and 0% inhibition respectively. Data are
622 presented as the mean \pm SD of four technical replicates. A control reaction with increasing concentrations of
623 Mac1 indicated that <50% of the mono-ADP-ribosylated PARP10 was hydrolyzed in the 0% inhibition control
624 (**Supplementary Figure 2**). In addition, a counterscreen to test for NUDT5 inhibition or assay interference
625 was performed with identical reactions, except Mac1 was omitted and ADP-ribose was added to a final
626 concentration of 2 μ M (Sigma, A0752).

627

628 **HTRF:**

629 Binding of the compounds to macrodomain proteins was assessed by the displacement of an ADPr
630 conjugated biotin peptide from His₆-tagged protein using an HTRF-technology based screening assay which
631 was performed as previously described (Schuller et al. 2021). The protein sequences used for SARS-CoV-2
632 Mac1, and the human macrodomains TARG1 and MacroD2, are listed in **Supplementary Table 5**. All
633 proteins were expressed and purified as described previously for SARS-CoV-2 Mac1 (Schuller et al. 2021).
634 Compounds were dispensed into ProxiPlate-384 Plus (PerkinElmer) assay plates using an Echo 650 Liquid
635 Handler (Beckman Coulter). Binding assays were conducted in a final volume of 16 μ l with 12.5 nM NSP3
636 Mac1 protein, 200 nM peptide ARTK(Bio)QTARK(Aoa- RADP)S (Cambridge Peptides), 1:20000 Eu³⁺ cryptate
637 conjugated to a His₆-specific antibody (HTRF donor, PerkinElmer AD0402) and 1:500 Streptavidin-XL665
638 (HTRF acceptor, PerkinElmer 610SAXLB) in assay buffer (25 mM 4-(2-hydroxyethyl)-1-piperazine-1-
639 ethanesulfonic acid (HEPES) pH 7.0, 20 mM NaCl, 0.05% bovine serum albumin and 0.05% Tween-20).
640 TARG1 and MacroD2 binding were measured at 25nM and 12.5 nM, respectively. Assay reagents were
641 dispensed manually into plates using an electronic multichannel pipette. Macrodomain protein and peptide
642 were dispensed and preincubated for 30 min at room temperature before HTRF reagents were added.
643 Fluorescence was measured after a 1 hour incubation at room temperature using a Perkin Elmer EnVision
644 2105-0010 Dual Detector Multimode microplate reader with dual emission protocol (A = excitation of 320 nm,
645 emission of 665 nm, and B = excitation of 320 nm, emission of 620 nm). Compounds were tested in triplicate
646 in a 14-point dose response. Raw data were processed to give an HTRF ratio (channel A/B \times 10,000), which
647 was used to generate IC₅₀ curves. The IC₅₀ values were determined by nonlinear regression using GraphPad
648 Prism (version 10.1.1). Data are presented as mean \pm SD of three technical replicates.

649

650 **CETSA:**

651 Cellular target engagement of compounds was assessed using a CETSA-nLuc or CETSA-WB assay
652 (Martinez et al. 2018). The SARS-CoV-2 Mac1 macrodomain was cloned into pcDNA3.1 by Genscript with
653 both an N-terminal 3XFLAG tag and a C-terminal HiBiT tag as listed in **Supplementary Table 5**. A 2A mKate

654 was included to identify successfully transfected cells (e.g., pcDNA-3xFLAG-Mac1^{WT}-nLuc-t2A-mKate2).
655 Plasmids were reverse transfected into A549 cells using Lipofectamine 3000 transfection reagent (Thermo).
656 After 48 h, cells were harvested by trypsinization and resuspended at 1×10^6 cells/ml in CETSA buffer ($1 \times$
657 DPBS (with CaCl₂ and MgCl₂), 1 g/l glucose and $1 \times$ protease inhibitor cocktail (Roche, 5892970001). Cells
658 were treated in microcentrifuge tubes with compound or DMSO and incubated at 37°C for 1 h.

659

660 For CETSA-nLuc experiments, 30 μ l of suspended cells were dispensed into a 96-well PCR plate (Biorad)
661 and heated for 3.5 min using a preheated gradient thermal cycler (Eppendorf). A Nano-Glo® HiBiT Lytic
662 Detection System (Promega) was used to quantify HiBiT-tagged proteins in cell lysates. 30 μ l of a mixture
663 containing Lytic Buffer, LgBiT protein, HiBiT Lytic Substrate were added to the cell suspension, and
664 luminescence intensity was measured using a Biotek Synergy H1. Luminescence values for each sample
665 were normalized to the lowest temperature on the range and T_{agg} (T-aggregate) values were determined by
666 fitting data with a four-parameter sigmoidal dose-response equation using non-linear regression in GraphPad
667 Prism (version 10.1.1). Delta values were calculated by subtracting the T_{agg}^{DMSO} value from the T_{agg}^{drug} value.
668 Data are presented as mean \pm SD of two technical replicates.

669

670 For CETSA-WB experiments, 45 μ l of suspended cells were dispensed into PCR strip tubes and heated for
671 3.5 min using a pre-heated gradient thermal cycler (Eppendorf). Samples were then placed in an aluminum
672 PCR block on a dry ice/ethanol bath for 3 min, followed by incubating at 37°C for 3 min, and vortexing for 3
673 seconds. This freeze-thaw cycle was repeated three more times. Insoluble proteins were transferred to a 1.5
674 ml microcentrifuge tube, separated by centrifugation (20,000g, 15 min, 4°C) and 40 μ l of supernatant
675 corresponding to soluble proteins was kept for WB. Samples were separated on an SDS-polyacrylamide gel
676 and transferred to a PVDF membrane. The following antibodies were used for immunoblotting: anti-FLAG
677 antibody (Sigma, F1804, 1:1000 overnight), anti-mouse HRP antibody (CST, 7076S, 1:3000 for 1 hour).
678 Images were captured using the Azure c600 Western Blot Imaging System, quantified using ImageJ and
679 plotted as above.

680

681 Cellular and Organoid studies

682 SARS-CoV-2 culture:

683 As described in our previous report (Taha et al. 2023b), the pBAC SARS-CoV-2 WT (WA1) and N40D mutant
684 constructs on WA1 background were made by co-transfecting them with an N expression vector into BHK-21
685 cells. Following three days of transfection the cell supernatants were used to infect Vero cells stably
686 expressing TMPRSS2, followed by passaging to achieve a high viral titer. All viruses generated or used in
687 this study were verified by NGS using the ARTIC Network's protocol. A previously reported mNeon SARS-
688 CoV-2 infectious clone (ic-SARS-CoV-2-mNG) (Xie et al. 2020) was passaged on Vero-TMPRSS2 and used
689 for Incucyte-based antiviral assays.

690

691 Cells:

692 BHK-21 obtained from ATCC, were grown in DMEM (Corning) with 10% fetal bovine serum (FBS)
693 (GeminiBio), $1 \times$ Glutamax (Corning), and $1 \times$ Penicillin-Streptomycin (Corning) at 37°C in a 5% CO₂
694 atmosphere. A549-ACE2h cells were generated by stably expressing hACE2 (Khalid et al. 2024) and further
695 selecting for high ACE2 expression levels via FACS with Alexa Fluor® 647 conjugated to a hACE2-specific
696 antibody (FAB9332R, R&D systems). These cells were cultured in DMEM supplemented with 10% FBS, 10
697 μ g/ml blasticidin (Sigma), $1 \times$ NEAA (Gibco), and 1% L-glutamine (Corning) at 37°C in a 5% CO₂ atmosphere.
698 Vero cells that stably overexpress human TMPRSS2 (Vero TMPRSS2), a gift from the Whelan lab (Case et
699 al. 2020), were cultured under the same conditions. Additionally, Vero cells that stably express human ACE2
700 and TMPRSS2 (VAT), provided by A. Creanga and B. Graham from the NIH, were maintained in DMEM with
701 10% FBS, $1 \times$ Penicillin-Streptomycin, and 10 μ g/ml puromycin at 37°C in a 5% CO₂ atmosphere. A549 cells
702 obtained from ATCC, were grown in DMEM Glutamax (Gibco) with 10% fetal bovine serum (FBS)
703 (GeminiBio), and $1 \times$ Penicillin-Streptomycin (Corning) at 37°C in a 5% CO₂ atmosphere.

704

705 **Human airway organoids:**

706 Human lung tissues were used to generate self-organizing 3D human airway organoids (HAO) consisting of
707 basal cells, multi-ciliated epithelial cells, mucus-producing secretory cells, and club cells. As described
708 previously (Suryawanshi et al. 2022; Taha et al. 2023b), the human lung tissues obtained from Matthay lab
709 were dissociated to single cells using enzymatic digestion. The isolated single cells were resuspended in
710 Basement Membrane Extract (BME, R&D biosystems), to form a BME droplet containing cells which was
711 submerged in HAO medium consisting 1 mM HEPES (Corning), 1× GlutaMAX (Gibco), 1× Penicillin-
712 Streptomycin (Corning), 10% R-spondin1 conditioned medium, 1% B27 (Gibco), 25 ng/ml noggin (Peprotech),
713 1.25 mM N-acetylcysteine (Sigma-Aldrich), 10 mM nicotinamide (Sigma-Aldrich), 5 nM heregulin-β1
714 (Peprotech), and 100 µg/ml Primocin (InvivoGen) in DMEM. This HAO medium was also supplemented with
715 5 µM Y-27632, 500 nM A83-01, 500 nM SB202190, 25 ng/ml FGF7, and 100 ng/ml FGF10 (all obtained from
716 Stem Cell Technologies). After sufficient growth of HAO's, in order to differentiate the HAO cells the HAO
717 medium was replaced with equal proportion of HAO medium and PneumaCult-ALI medium (Stem cell
718 Technologies).

719

720 **SARS-CoV-2 replicon assay:**

721 The SARS-CoV-2 replicon assay was conducted as described previously (Taha et al. 2023a, 2023b). Briefly,
722 the pBAC SARS-CoV-2 ΔSpike WT or nsp3 Mac1 N40D modified plasmids (40 µg), were transfected into
723 BHK-21 fibroblast cells along with N and S expression vectors (20 µg each) in a 15-cm² tissue culture dish.
724 The culture media was replaced with fresh growth medium 12 hours post-transfection. The media containing
725 single-round infectious particles was collected and 0.45 µm-filtered 72 hours post-transfection and stored at
726 -80 C until use.

727 Vero-ACE2-TMPRSS2 (VAT) and A549 ACE2^h cells were plated 2.5x10⁴ cells per well in 96-well plate in
728 media containing 0, 1000, or 10000 IU/ml of IFN-γ. After 16 hours, the media was replaced with 50 µl media
729 containing 5x the final desired concentration of IFN-γ and AVI-4206. After 2 hours, 200 µl of supernatant
730 containing WA1 or WA1 nsp3 Mac1 N40D single-round infectious particles was added. After 8 hours, the cells
731 were washed with 200 µl culture medium and 100 µl of culture medium was added. After 16 hours, 50 µl from
732 each well was transferred to a white 96-well plate to measure nanoluciferase activity by adding 50 µl of Nano-
733 Glo luciferase assay buffer and substrate and analyzed on an Infinite M Plex plate reader (Tecan).

734

735 **SARS-CoV-2 *in vitro* antiviral assay:**

736 Antiviral activity of compounds was assessed using the Incucyte® live-cell analysis system. 2x10⁴ A549-
737 ACE2h cells per well were seeded in Edge 2.0 96-well plates filled with 1.5 ml PBS in the outer moats and
738 100 µl in-between wells and incubated at 37°C and 5% CO₂. The next day, cells were pre-treated with
739 compounds for 2 hours, followed by the removal of the compounds and infection with 50 µl of icSARS-CoV-
740 2-mNG at a MOI 0.1 for 2 hours. Subsequently, virus inoculum was removed and fresh compounds diluted in
741 DMEM (10% FBS, 1% L-Glutamine, 1× P/S, 1× NEAA, Incucyte® Cytotox Dye) were added. Infected cells
742 were placed in an Incucyte S3 (Sartorius) and infection and cell death were measured over 48 hours at 1-
743 hour intervals using a 10x objective, capturing 3 images per well at each time point under cell maintenance
744 conditions (37°C, 5% CO₂). Infection and cell death were quantified as Total Green Object Integrated Intensity
745 (300 ms acquisition time) and Red Object Integrated Intensity (400 ms acquisition time), respectively. After
746 in-built software analysis, raw data was exported and antiviral efficacy was determined as the percentage of
747 viral replication normalized to the vehicle control. Nirmatrelvir (HY-138687, MedChemExpress) and
748 uninfected cells were used as intra-assay positive and negative controls, respectively. Unless otherwise
749 stated, experiments were conducted in triplicate with 3 technical replicates. EC₅₀ values were calculated using
750 GraphPad PRISM 10 (La Jolla, CA, USA) employing a dose-response inhibition equation with a non-linear fit
751 regression model.

752

753 **Antiviral efficacy in human airway organoids:**

754 The differentiated HAOs were utilized to analyze the dose-dependent anti SARS-CoV-2 efficacy of AVI-4206.
755 Briefly, 100,000 cells of differentiated HAOs were seeded in a V-bottom plate (Greiner Bio-One). The cells
756 were pretreated for 2 hours prior to infection with various concentrations of AVI-4206 (0, 0.16 μ M, 0.8 μ M, 4
757 μ M, 20 μ M, 100 μ M). After pretreatment, the HAOs were washed and infected with SARS-CoV-2 WA1 at a
758 multiplicity of infection (MOI) of 1. A WA1-N40D mutant strain lacking the macrodomain activity was used as
759 a positive control. Following 2 hours of infection, the HAOs were washed three times. Each washing step
760 involved replacing the media with PBS and centrifuging the cells at 1000 rpm for 3 minutes. After three
761 washes, the PBS was replaced with 100 μ l of HAO differentiation medium, with or without varying
762 concentrations of AVI-4206, and the plate was incubated for 72 hours at 37°C with 5% CO₂. Supernatants
763 collected at 24-hour intervals were used to analyze mature virus particle formation via plaque assay.

764

765 **Drug cytotoxicity assay:**

766 A549-ACE2h cells were seeded and incubated as for the in vitro antiviral assay. Cells were treated with
767 compounds at the respective concentrations and vehicle control for 50 hours at 37°C and 5% CO₂.
768 Subsequently, Cell Titer-Glo[®] reagent was added in a 1:1 ratio to the cells and incubated at room temperature
769 for 5 minutes before transferring 100 μ l of the mixture to a white 96-well plate. Luciferase activity was
770 measured using an Infinite M Plex plate reader (Tecan). Cell viability was determined as the percentage of
771 viability normalized to the vehicle control. Compound cytotoxicity was assessed in parallel with infection
772 experiments using cells of the same passage.
773

774 **Thermal proteome profiling (TPP) assay:**

775 Pelleted A549 cells were resuspended in extraction buffer (1 \times PBS + phosphatase and protease inhibitors
776 (phosSTOP (Roche) and cOmplete Mini Protease Inhibitor Cocktail (Roche)) with gentle pipetting followed by
777 rotation at 4°C for 30 minutes. Lysates were centrifuged at 1000g for 10 minutes at 4°C and supernatant was
778 transferred to new tubes. Recombinant Mac1 was spiked into lysate to a final concentration of 0.05 μ M.
779 Lysates + Mac1 were incubated with compound at a final concentration of 100 μ M AVI-4206 or DMSO for 30
780 minutes at 25°C. Lysates (2 replicates per condition) were distributed into 10 aliquots (20 μ l each) in PCR
781 tubes. Samples were heated from 37°C to 64°C in 3°C increments on a BioRad C1000 Touch Thermal cycler,
782 and held for four minutes at the specified temperature. Samples were held at room temperature for three
783 minutes. Samples were then subjected to 2 cycles of flash freezing and thawing at 35°C. Aggregated proteins
784 were removed by centrifugation at 20,000g for 60 minutes. 20 μ l of lysis buffer (8 M urea, 100 mM Tris, pH
785 ~7.5) was added to each well and samples were incubated for 30 minutes at room temperature. Samples
786 were reduced and alkylated by the addition of TCEP (100mM final) and 2-chloroacetamide (44mM final)
787 followed by incubation at room temperature for 30 minutes. Urea concentration was diluted to 1 M by the
788 addition of 100 mM tris (pH ~7.5). Samples were digested overnight with LysC (Wako, 1:100 enzyme: protein
789 ratio) and trypsin (Promega, 1:50 enzyme:protein ratio). Samples were desalted with a 96-well mini 20MG
790 PROTO 300 C18 plate (HNS S18V, The Nest Group) according to manufacturer's directions. Peptide
791 concentration was determined by NanoDrop (Thermo).

792 Following digestion, peptides were injected onto a timsTOF SCP (Bruker) connected to either an EASY-nLC
793 1200 system (Thermo) or VanquishNeo (Thermo). Peptides were separated on a PepSep reverse-phase C18
794 column (1.9 μ m particles, 15 cm, 150 mm ID) (Bruker) with a gradient of 5-28% buffer B (0.1% formic acid in
795 acetonitrile) over buffer A (0.1% formic acid in water) over 20 minutes, an increase to 32% B in 3 minutes,
796 and held at 95% B for 7 minutes. DIA-PASEF analyses were acquired from 100 to 1700 m/z over a 1/K θ of
797 0.70 to 1.30 Vs/cm², with a ramp and accumulation time set to 75 ms. Library DDA PASEF runs were collected
798 over the same m/z and 1/K θ range and a cycle time of 1.9 s.

799 All data was searched against the Uniprot Human database (downloaded 05/25/23) appended with the SARS-
800 CoV-2 database (downloaded 02/20/2024) using a combined DDA and DIA library in Spectronaut (Biognosys,
801 version 19.0). Default settings, including trypsin digestion, variable modifications of methionine oxidation and
802 N-termini acetylation, and fixed modification of cysteine carbamidomethylation, were used. Missing values
803 were imputed for each run using background intensity. Data was filtered to obtain a false discovery rate of

804 1% at the peptide spectrum match and protein level. Lysate experiments were normalized to the lowest
805 temperature (37°C) and melting points were determined in R using the Inflect package (McCracken et al.
806 2021).

807 PK and *In vivo* studies

808 **ADMET target and kinase studies:**

809 The kinase assessment was performed using contract services by Eurofins using their scanEDGE
810 KINOMEScan Assay Platform (Study Code: US073-0032699). Assessment of ADMET targets (cardiac
811 channel profiling, CYP induction, peptidase selectivity panel and secondary pharmacology profiling) was
812 performed via NIAID's suite of preclinical services for in vitro assessment (Contract No.
813 HHSN272201800007I/75N93022F00001).

814 **Pharmacokinetic Studies:**

815 The pharmacokinetic study of AVI-4206 with IV (10 mg/kg), PO (50 mg/kg), and IP (100 mg/kg) dosing (Fig. 4B and
816 Supplementary Table 2) was performed in male CD1 mice (n = 3 per group) using a formulation of 10% DMSO: 50%
817 PEG 400: 40% of a 20% HP-β-CD in water. Microsampling (40 µl) via facial vein was performed at 0, 0.083, 0.25, 0.5,
818 1, 2, 4, 8, and 24 h into K₂EDTA tubes. The blood samples were collected and centrifuged to obtain plasma (8000 rpm,
819 5 min) within 15 minutes post sampling. Nine blood samples were collected from each mouse; three samples were
820 collected for each time point. Data was processed by Phoenix WinNonlin (version 8.3); samples below the limit of
821 quantitation were excluded in the PK parameters and mean concentration calculation.

822 **Animal experiments:**

823 All the mice experiments were approved (AN169239-01) by the Institutional Animal Care and Use committees
824 at the University of California, San Francisco and Gladstone Institutes and performed in strict accordance
825 with the National Institutes of Health Guide for the Care and Use of Laboratory Animal. For screening of lead
826 Macrodomein inhibitors we employed a transgenic mice model capable of expressing human ACE2. Female
827 mice were divided into three groups: test, positive control, and negative control. The positive control groups
828 were infected (5×10^2 PFUs) with the N40D mutant of SARS-CoV-2, while the other mice were infected with
829 the WA1 strain. Intraperitoneal treatments were administered twice daily which began at a day prior infection
830 and continued until 5 days post-infection, with close monitoring for disease parameters such as weight loss,
831 hypothermia, and hunched posture. At 4 and 7 days post-infection, a subset of mice from each group was
832 euthanized, and their lungs and brain tissues were harvested for virus titration by plaque assay and cytokine
833 expression.

834 **Plaque assay:**

835 The mature virus particles in the lung homogenates were analyzed using plaque assay. Briefly, VAT cells
836 were seeded in a 12-well plate and incubated overnight. The cells were inoculated with 10 to 10⁶ dilutions of
837 the respective lung homogenates. After 1h incubation, the lung homogenates in the wells were overlaid with
838 2.5% Avicel (RC-591, Dupont). And the plates were incubated at 37°C and 5% CO₂ for 48h. After incubation
839 the overlay media was removed and the cells were fixed in 10% formalin. The plaques were visualized by
840 staining the cells with crystal violet. Data analysis was performed by using GraphPad Prism version 10.

841 **Cytokine estimation:**

842 Lung homogenates were clarified by centrifugation at 6000 rpm for 10 mins and were used for enzyme linked
843 immunosorbent assay (ELISA) based cytokine estimation. The assays were performed as per manufacturer's
844 protocol for IP-10 (Invitrogen, catalog#BMS56018 and BMS6018TEN), IL-2 (Invitrogen, catalog#BMS601,
845 and BMS601TEN), IL-6 (Invitrogen, catalog#BMS103-2, BMS603-2TWO, and BMS603-2TEN), TNF-α
846 (Invitrogen, catalog#BMS607-3 and BMS607-3TEN), IL1b (Invitrogen, catalog#BMS6002-2 and BMS6002-
847 2TEN).

848 Data and Materials Availability

849 X-ray structures have been deposited in the Protein Data Bank as: 9CXY (AVI-1500), 9CXZ (AVI-1501),
850 7HC4 (AVI-3367), 7HC5 (AVI-3765), 7HC6 (AVI-3764), 7HC7 (AVI-4051), 7HC8 (AVI-3763), 7HC9 (AVI-
851 3762), 7HCA (AVI-4636), 9CY0 (AVI-4206).

852 All other data supporting the findings of the present study are available in the article, extended data and
853 supplementary figures, or are available from the corresponding authors on request.

854

855 Competing Interests

856 A.R.R., P.J., R.L.G., T.T., M.R., J.S.F., G.J.C., B.K.S., R.J.N., A.A., M.D., P.C.O., Y.D.P., N.K., M.O., T.Y.T.,
857 R.S., F.Z.B., and M.M. are listed as inventors on a patent application describing small molecule macrodomain
858 inhibitors, which includes compounds described herein. T.Y.T and M.O. are listed as inventors on a patent
859 application filed by the Gladstone Institutes that covers the use of pGLUE to generate SARS-CoV-2 infectious
860 clones and replicons.

861

862 The Krogan laboratory has received research support from Vir Biotechnology, F. Hoffmann-La Roche and
863 Rezo Therapeutics. N.J.K. has financially compensated consulting agreements with Maze Therapeutics and
864 Interline Therapeutics. He is on the Board of Directors and is President of Rezo Therapeutics and is a
865 shareholder in Tenaya Therapeutics, Maze Therapeutics, Rezo Therapeutics, GEn1E Lifesciences and
866 Interline Therapeutics. B.K.S is co-founder of BlueDolphin LLC, Epiodyne Inc, and Deep Apple Therapeutics,
867 Inc., and serves on the SRB of Genentech, the SAB of Schrodinger LLC, and the SAB of Vilya Therapeutics.
868 M.O. is a cofounder of Directbio and board member of InVisishield. A.R.R. is a co-founder of TheRas, Elgia
869 Therapeutics, and Tataara Therapeutics, and receives sponsored research support from Merck, Sharp and
870 Dohme. A.A. is a co-founder of Tango Therapeutics, Azkarra Therapeutics and Kytarro; a member of the
871 board of Cytomx, Ovibio Corporation, Cambridge Science Corporation; a member of the scientific advisory
872 board of Genentech, GLAdiator, Circle, Bluestar/Clearnote Health, Earli, Ambagon, Phoenix Molecular
873 Designs, Yingli/280Bio, Trial Library, ORIC and HAP10; a consultant for ProLynx, Next RNA and Novartis;
874 receives research support from SPARC; and holds patents on the use of PARP inhibitors held jointly with
875 AstraZeneca from which he has benefited financially (and may do so in the future). J.S.F. is a consultant to,
876 shareholder of, and receives sponsored research support from Relay Therapeutics.

877

878

879 References

880 Alhammad YM, Parthasarathy S, Ghimire R, Kerr CM, O'Connor JJ, Pfannenstiel JJ, et al. SARS-CoV-2
881 Mac1 is required for IFN antagonism and efficient virus replication in cell culture and in mice. *Proc Natl*
882 *Acad Sci U S A*. 2023 Aug 29;120(35):e2302083120.

883 Bao L, Deng W, Huang B, Gao H, Liu J, Ren L, et al. The pathogenicity of SARS-CoV-2 in hACE2
884 transgenic mice. *Nature*. 2020 Jul;583(7818):830–3.

885 Case JB, Rothlauf PW, Chen RE, Liu Z, Zhao H, Kim AS, et al. Neutralizing Antibody and Soluble ACE2
886 Inhibition of a Replication-Competent VSV-SARS-CoV-2 and a Clinical Isolate of SARS-CoV-2. *Cell*
887 *Host Microbe*. 2020 Sep 9;28(3):475–85.e5.

888 Collins PM, Ng JT, Talon R, Nekrosiute K, Krojer T, Douangamath A, et al. Gentle, fast and effective crystal
889 soaking by acoustic dispensing. *Acta Crystallogr D Struct Biol*. 2017 Mar 1;73(Pt 3):246–55.

890 Correy GJ, Kneller DW, Phillips G, Pant S, Russi S, Cohen AE, et al. The mechanisms of catalysis and
891 ligand binding for the SARS-CoV-2 NSP3 macrodomain from neutron and x-ray diffraction at room

- 892 temperature. *Sci Adv.* 2022 May 27;8(21):eabo5083.
- 893 Dasovich M, Leung AKL. PARPs and ADP-ribosylation: Deciphering the complexity with molecular tools.
894 *Mol Cell.* 2023 May 18;83(10):1552–72.
- 895 Dasovich M, Zhuo J, Goodman JA, Thomas A, McPherson RL, Jayabalan AK, et al. High-Throughput
896 Activity Assay for Screening Inhibitors of the SARS-CoV-2 Mac1 Macrodomein. *ACS Chem Biol*
897 [Internet]. 2021 Dec 14; Available from: <http://dx.doi.org/10.1021/acscchembio.1c00721>
- 898 von Delft A, Hall MD, Kwong AD, Purcell LA, Saikatendu KS, Schmitz U, et al. Accelerating antiviral drug
899 discovery: lessons from COVID-19. *Nat Rev Drug Discov.* 2023 Jul;22(7):585–603.
- 900 Evans PR, Murshudov GN. How good are my data and what is the resolution? *Acta Crystallogr D Biol*
901 *Crystallogr.* 2013 Jul;69(Pt 7):1204–14.
- 902 Gahbauer S, Correy GJ, Schuller M, Ferla MP, Doruk YU, Rachman M, et al. Iterative computational design
903 and crystallographic screening identifies potent inhibitors targeting the Nsp3 macrodomain of SARS-
904 CoV-2. *Proc Natl Acad Sci U S A.* 2023 Jan 10;120(2):e2212931120.
- 905 Kabsch W. XDS. *Acta Crystallogr D Biol Crystallogr.* 2010 Feb;66(Pt 2):125–32.
- 906 Kar P, Chatrin C, Đukić N, Suyari O, Schuller M, Zhu K, et al. PARP14 and PARP9/DTX3L regulate
907 interferon-induced ADP-ribosylation. *EMBO J* [Internet]. 2024 Jun 4; Available from:
908 <http://dx.doi.org/10.1038/s44318-024-00126-0>
- 909 Kasson S, Dharmapriya N, Kim IK. Selective monitoring of the protein-free ADP-ribose released by ADP-
910 ribosylation reversal enzymes. *PLoS One.* 2021 Jun 30;16(6):e0254022.
- 911 Kerr CM, Parthasarathy S, Schwarting N, O'Connor JJ, Pfannenstiel JJ, Giri E, et al. PARP12 is required to
912 repress the replication of a Mac1 mutant coronavirus in a cell- and tissue-specific manner. *J Virol.* 2023
913 Sep 28;97(9):e0088523.
- 914 Kerr CM, Pfannenstiel JJ, Alhammad YM, O'Connor JJ, Ghimire R, Shrestha R, et al. Mutation of a highly
915 conserved isoleucine residue in loop 2 of several β -coronavirus macrodomains indicates that enhanced
916 ADP-ribose binding is detrimental to infection. *bioRxiv* [Internet]. 2024 Jul 12; Available from:
917 <http://dx.doi.org/10.1101/2024.01.03.574082>
- 918 Khalid MM, Chen IP, Soveg FS, Taha TY, Tabata T, Suryawanshi RK, et al. Regulation of virion production
919 by the ORF8 signal peptide across SARS-CoV-2 variants [Internet]. *bioRxiv.* 2024 [cited 2024 Jul 22].
920 p. 2024.03.05.583578. Available from: <https://www.biorxiv.org/content/10.1101/2024.03.05.583578v1>
- 921 Kim YM, Shin EC. Type I and III interferon responses in SARS-CoV-2 infection. *Exp Mol Med.* 2021
922 May;53(5):750–60.
- 923 Lee AA, Amick I, Aschenbrenner JC, Barr HM, Benjamin J, Brandis A, et al. Discovery of potent SARS-
924 CoV-2 nsp3 macrodomain inhibitors uncovers lack of translation to cellular antiviral response [Internet].
925 *bioRxiv.* 2024 [cited 2024 Aug 27]. p. 2024.08.19.608619. Available from:
926 <https://www.biorxiv.org/content/10.1101/2024.08.19.608619v1.abstract>
- 927 Leung AKL, Griffin DE, Bosch J, Fehr AR. The Conserved Macrodomein Is a Potential Therapeutic Target
928 for Coronaviruses and Alphaviruses. *Pathogens* [Internet]. 2022 Jan 14;11(1). Available from:
929 <http://dx.doi.org/10.3390/pathogens11010094>
- 930 Li C, Huang J, Yu Y, Wan Z, Chiu MC, Liu X, et al. Human airway and nasal organoids reveal escalating
931 replicative fitness of SARS-CoV-2 emerging variants. *Proc Natl Acad Sci U S A.* 2023a Apr
932 25;120(17):e2300376120.

- 933 Liebschner D, Afonine PV, Baker ML, Bunkóczi G, Chen VB, Croll TI, et al. Macromolecular structure
934 determination using X-rays, neutrons and electrons: recent developments in Phenix. *Acta Crystallogr D*
935 *Struct Biol.* 2019 Oct 1;75(Pt 10):861–77.
- 936 Li G, Hilgenfeld R, Whitley R, De Clercq E. Therapeutic strategies for COVID-19: progress and lessons
937 learned. *Nat Rev Drug Discov.* 2023b Jun;22(6):449–75.
- 938 Lord CJ, Ashworth A. PARP inhibitors: Synthetic lethality in the clinic. *Science.* 2017 Mar
939 17;355(6330):1152–8.
- 940 Martinez NJ, Asawa RR, Cyr MG, Zakharov A, Urban DJ, Roth JS, et al. A widely-applicable high-
941 throughput cellular thermal shift assay (CETSA) using split Nano Luciferase. *Sci Rep.* 2018 Jun
942 21;8(1):9472.
- 943 McCoy AJ, Grosse-Kunstleve RW, Adams PD, Winn MD, Storoni LC, Read RJ. Phaser crystallographic
944 software. *J Appl Crystallogr.* 2007 Aug 1;40(Pt 4):658–74.
- 945 McCracken NA, Peck Justice SA, Wijeratne AB, Mosley AL. Inflect: Optimizing Computational Workflows for
946 Thermal Proteome Profiling Data Analysis. *J Proteome Res.* 2021 Apr 2;20(4):1874–88.
- 947 McPherson RL, Abraham R, Sreekumar E, Ong SE, Cheng SJ, Baxter VK, et al. ADP-ribosylhydrolase
948 activity of Chikungunya virus macrodomain is critical for virus replication and virulence. *Proc Natl Acad*
949 *Sci U S A.* 2017 Feb 14;114(7):1666–71.
- 950 Michalska K, Kim Y, Jedrzejczak R, Maltseva NI, Stols L, Endres M, et al. Crystal structures of SARS-CoV-
951 2 ADP-ribose phosphatase: from the apo form to ligand complexes. *IUCrJ.* 2020 Sep 1;7(Pt 5):814–24.
- 952 Minkoff JM, tenOever B. Innate immune evasion strategies of SARS-CoV-2. *Nat Rev Microbiol.* 2023
953 Mar;21(3):178–94.
- 954 Neufeldt CJ, Cerikan B, Cortese M, Frankish J, Lee JY, Plociennikowska A, et al. SARS-CoV-2 infection
955 induces a pro-inflammatory cytokine response through cGAS-STING and NF- κ B. *Commun Biol.* 2022
956 Jan 12;5(1):45.
- 957 O'Connor JJ, Ferraris D, Fehr AR. An Update on the Current State of SARS-CoV-2 Mac1 Inhibitors.
958 *Pathogens* [Internet]. 2023 Oct 7;12(10). Available from: <http://dx.doi.org/10.3390/pathogens12101221>
- 959 Oladunni FS, Park JG, Pino PA, Gonzalez O, Akhter A, Allué-Guardia A, et al. Lethality of SARS-CoV-2
960 infection in K18 human angiotensin-converting enzyme 2 transgenic mice. *Nat Commun.* 2020 Nov
961 30;11(1):6122.
- 962 Papini C, Ullah I, Ranjan AP, Zhang S, Wu Q, Spasov KA, et al. Proof-of-concept studies with a
963 computationally designed M^{pro} inhibitor as a synergistic combination regimen alternative to Paxlovid.
964 *Proc Natl Acad Sci U S A.* 2024 Apr 23;121(17):e2320713121.
- 965 Parthasarathy S, Saenjamsai P, Hao H, Ferkul A, Pfannenstiel JJ, Suder EL, et al. PARP14 is pro- and anti-
966 viral host factor that promotes IFN production and affects the replication of multiple viruses. *bioRxiv*
967 [Internet]. 2024 Apr 26; Available from: <http://dx.doi.org/10.1101/2024.04.26.591186>
- 968 Pearce NM, Krojer T, Bradley AR, Collins P, Nowak RP, Talon R, et al. A multi-crystal method for extracting
969 obscured crystallographic states from conventionally uninterpretable electron density. *Nat Commun.*
970 2017 Apr 24;8:15123.
- 971 Plataniias LC. Mechanisms of type-I- and type-II-interferon-mediated signalling. *Nat Rev Immunol.* 2005
972 May;5(5):375–86.

- 973 Robertson SJ, Bedard O, McNally KL, Shaia C, Clancy CS, Lewis M, et al. Genetically diverse mouse
974 models of SARS-CoV-2 infection reproduce clinical variation in type I interferon and cytokine responses
975 in COVID-19. *Nat Commun.* 2023 Jul 25;14(1):4481.
- 976 Sachs N, Papaspyropoulos A, Zomer-van Ommen DD, Heo I, Böttinger L, Klay D, et al. Long-term
977 expanding human airway organoids for disease modeling. *EMBO J [Internet]*. 2019 Feb 15;38(4).
978 Available from: <http://dx.doi.org/10.15252/embj.2018100300>
- 979 Savitski MM, Reinhard FBM, Franken H, Werner T, Savitski MF, Eberhard D, et al. Tracking cancer drugs in
980 living cells by thermal profiling of the proteome. *Science.* 2014 Oct 3;346(6205):1255784.
- 981 Schuller M, Correy GJ, Gahbauer S, Fearon D, Wu T, Díaz RE, et al. Fragment binding to the Nsp3
982 macrodomain of SARS-CoV-2 identified through crystallographic screening and computational docking.
983 *Sci Adv [Internet]*. 2021 Apr;7(16). Available from: <http://dx.doi.org/10.1126/sciadv.abf8711>
- 984 Schuller M, Zarganes-Tzitzikas T, Bennett J, De Cesco S, Fearon D, von Delft F, et al. Discovery and
985 Development Strategies for SARS-CoV-2 NSP3 Mac1 Domain Inhibitors. *Pathogens [Internet]*. 2023
986 Feb 15;12(2). Available from: <http://dx.doi.org/10.3390/pathogens12020324>
- 987 Simoneau CR, Chen PY, Xing GK, Hayashi JM, Chen IP, Khalid MM, et al. NF- κ B inhibitor alpha controls
988 SARS-CoV-2 infection in ACE2-overexpressing human airway organoids. *Sci Rep.* 2024 Jul
989 4;14(1):15351.
- 990 Slade D. PARP and PARG inhibitors in cancer treatment. *Genes Dev.* 2020 Mar 1;34(5-6):360–94.
- 991 Suryawanshi RK, Chen IP, Ma T, Syed AM, Brazer N, Saldhi P, et al. Limited cross-variant immunity from
992 SARS-CoV-2 Omicron without vaccination. *Nature.* 2022 Jul;607(7918):351–5.
- 993 Taha TY, Chen IP, Hayashi JM, Tabata T, Walcott K, Kimmerly GR, et al. Rapid assembly of SARS-CoV-2
994 genomes reveals attenuation of the Omicron BA.1 variant through NSP6. *Nat Commun.* 2023a Apr
995 21;14(1):2308.
- 996 Taha TY, Suryawanshi RK, Chen IP, Correy GJ, McCavitt-Malvido M, O’Leary PC, et al. A single
997 inactivating amino acid change in the SARS-CoV-2 NSP3 Mac1 domain attenuates viral replication in
998 vivo. *PLoS Pathog.* 2023b Aug;19(8):e1011614.
- 999 Tan B, Zhang X, Ansari A, Jadhav P, Tan H, Li K, et al. Design of a SARS-CoV-2 papain-like protease
000 inhibitor with antiviral efficacy in a mouse model. *Science.* 2024 Mar 29;383(6690):1434–40.
- 001 Voth LS, O’Connor JJ, Kerr CM, Doerger E, Schwarting N, Sperstad P, et al. Unique Mutations in the
002 Murine Hepatitis Virus Mac1 Domain Differentially Attenuate Virus Replication, Indicating Multiple Roles
003 for the Mac1 Domain in Coronavirus Replication. *J Virol.* 2021 Jul 12;95(15):e0076621.
- 004 Wazir S, Parviainen TAO, Pfannenstiel JJ, Duong MTH, Cluff D, Sowa ST, et al. Discovery of 2-Amide-3-
005 methylester Thiophenes that Target SARS-CoV-2 Mac1 and Repress Coronavirus Replication,
006 Validating Mac1 as an Antiviral Target. *J Med Chem.* 2024 Apr 25;67(8):6519–36.
- 007 Xie X, Muruato A, Lokugamage KG, Narayanan K, Zhang X, Zou J, et al. An Infectious cDNA Clone of
008 SARS-CoV-2. *Cell Host Microbe.* 2020 May 13;27(5):841–8.e3.
- 009 Zheng J, Wong LYR, Li K, Verma AK, Ortiz ME, Wohlford-Lenane C, et al. COVID-19 treatments and
010 pathogenesis including anosmia in K18-hACE2 mice. *Nature.* 2021 Jan;589(7843):603–7.
- 011 Tino W. Sanchez, Michael H. Ronzetti, Ashley E. Owens, Maria Antony, Ty Voss, Eric Wallgren, Daniel
012 Talley, Krishna Balakrishnan, Sebastian E. Leyes Porello, Ganesha Rai, Juan J. Marugan, Samuel G.
013 Michael, Bolormaa Baljinnyam, Noel Southall, Anton Simeonov, and Mark J. Henderson. 2022. “Real-

014 Time Cellular Thermal Shift Assay to Monitor Target Engagement". *ACS Chemical Biology* 17 (9),
015 2471-2482
016 DOI: 10.1021/acscchembio.2c00334
017
018

019 **Supplementary information**

020 **Supplementary Table1 - X-ray data collection and refinement deposition statistics.**

Ligand	AVI-1500	AVI-1501	AVI-3367	AVI-3765	AVI-3764	AVI-4051	AVI-3763	AVI-3762	AVI-4636	AVI-4206	
PDB code	9CXY	9CXZ	7HC4	7HC5	7HC6	7HC7	7HC8	7HC9	7HCA	9CY0	
Beam line	ALS	ALS	ALS	ALS	ALS	ALS	SSRL 9-2	SSRL 9-2	ALS	ALS	
Wavelength (Å)	8.3.1	8.3.1	8.3.1	8.3.1	8.3.1	8.3.1	8.3.1	8.3.1	8.3.1	8.3.1	
Resolution range (Å)	0.88557 (0.88557)	0.88557 (0.88557)	0.88557 (0.88557)	0.88557 (0.88557)	0.88557 (0.88557)	0.88557 (0.88557)	0.88557 (0.88557)	0.88557 (0.88557)	0.88557 (0.88557)	0.88557 (0.88557)	
Space group	P4 ₃	P4 ₃	P4 ₃	P4 ₃	P4 ₃	P4 ₃	P4 ₃	P4 ₃	P4 ₃	P1	
Unit cell (α β γ, a b c)	88.8 88.8 39.5 90 90 90	88.9 88.9 39.4 90 90 90	88.8 88.8 39.5 90 90 90	88.8 88.8 39.5 90 90 90	88.8 88.8 39.6 90 90 90	88.8 88.8 39.4 90 90 90	88.8 88.8 39.6 90 90 90	88.8 88.8 39.6 90 90 90	88.8 88.8 39.6 90 90 90	88.9 88.9 39.3 90 90 90	30.3 39.8 64.4 89.9 77.8 90.1
Total reflections	925861 (88714)	1019499 (92950)	1052667 (79477)	1095419 (68284)	981382 (94605)	1075242 (76799)	1049402 (101219)	934650 (89428)	996315 (94266)	420519 (10537)	
Unique reflections	151957 (14738)	156086 (15234)	165160 (15511)	175278 (16099)	152839 (14932)	169798 (16087)	161313 (15833)	142525 (13787)	151748 (14847)	235488 (6157)	
Multiplicity	6.1 (5.9)	6.5 (6.1)	6.4 (5.1)	6.2 (4.1)	6.4 (6.3)	6.3 (4.7)	6.5 (6.3)	6.6 (6.4)	6.6 (6.3)	1.8 (1.7)	
Completeness (%)	99.51 (96.98)	99.59 (97.52)	99.30 (93.65)	99.13 (91.70)	99.77 (98.28)	99.44 (94.83)	99.70 (98.49)	98.59 (96.15)	99.74 (98.30)	75.89 (19.87)	
Mean I/sigma(I)	13.96 (0.68)	15.02 (1.04)	13.32 (0.77)	11.98 (0.58)	9.03 (0.70)	12.87 (0.79)	12.16 (0.64)	10.78 (0.66)	13.86 (0.67)	13.15 (1.22)	
Wilson B-factor	13.38	12.91	12.4	12.14	11.92	12.15	11.98	12.53	14.12	6.69	
R-merge	0.0459 (2.25)	0.0439 (1.39)	0.0489 (1.38)	0.0546 (1.61)	0.0789 (1.73)	0.0521 (1.34)	0.0589 (2.38)	0.0672 (2.3)	0.0458 (2.24)	0.0334 (0.463)	
R-meas	0.0503 (2.47)	0.0477 (1.52)	0.0532 (1.54)	0.0594 (1.85)	0.0860 (1.88)	0.0567 (1.5)	0.0640 (2.60)	0.0730 (2.51)	0.0498 (2.44)	0.0472 (0.655)	
R-pim	0.0203 (0.995)	0.0184 (0.607)	0.0207 (0.665)	0.0233 (0.879)	0.0337 (0.751)	0.0222 (0.669)	0.0249 (1.03)	0.0282 (0.979)	0.0193 (0.961)	0.0334 (0.463)	
CC _{1/2}	0.999 (0.463)	0.999 (0.709)	0.999 (0.547)	0.999 (0.405)	0.999 (0.537)	0.999 (0.582)	0.999 (0.466)	0.999 (0.484)	0.999 (0.424)	0.997 (0.643)	
CC*	1 (0.795)	1 (0.911)	1 (0.841)	1 (0.759)	1 (0.836)	1 (0.858)	1 (0.797)	1 (0.808)	1 (0.772)	0.999 (0.885)	
Reflections used in refinement	151730 (14738)	156007 (15234)	164947 (15512)	174746 (16099)	152688 (14932)	169673 (16087)	161090 (15833)	142225 (13787)	151557 (14847)	235328 (6157)	
Reflections used for R-free	7357 (789)	7525 (740)	7958 (711)	8434 (781)	7391 (787)	8190 (751)	7762 (741)	6888 (690)	7340 (790)	11753 (303)	
R-work	0.1436 (0.4057)	0.1432 (0.3464)	0.1416 (0.4193)	0.1434 (0.4132)	0.1439 (0.4514)	0.1423 (0.3854)	0.1502 (0.4026)	0.1549 (0.5311)	0.1552 (0.3774)	0.1620 (0.2952)	
R-free	0.1609 (0.4006)	0.1594 (0.3372)	0.1583 (0.4254)	0.1587 (0.3953)	0.1595 (0.4464)	0.1580 (0.3611)	0.1686 (0.3973)	0.1773 (0.5333)	0.1735 (0.3805)	0.1884 (0.2959)	
CC(work)	0.977 (0.759)	0.975 (0.874)	0.975 (0.807)	0.975 (0.741)	0.975 (0.823)	0.974 (0.825)	0.974 (0.785)	0.974 (0.716)	0.972 (0.737)	0.954 (0.799)	
CC(free)	0.971 (0.779)	0.974 (0.881)	0.967 (0.823)	0.965 (0.777)	0.966 (0.750)	0.969 (0.847)	0.963 (0.779)	0.964 (0.677)	0.964 (0.753)	0.933 (0.763)	
Number of non-hydrogen atoms	3082	3046	3759	3756	3658	3675	3488	3811	4148	6135	
Number of atoms											
macromolecules	2609	2615	3260	3253	3162	3177	2992	3315	3644	5240	
ligands	35	31	45	37	37	47	43	43	39	204	
solvent	446	406	472	480	473	470	469	469	481	783	
Protein residues	338	338	337	336	336	336	336	337	337	336	
RMS											
Bonds (Å)	0.175	0.144	0.038	0.006	0.006	0.006	0.006	0.11	0.056	0.317	
Angles (°)	3.98	3.8	1.3	0.98	0.96	0.95	0.98	2.27	1.71	5.69	
Ramachandran											
Favored (%)	99.1	98.8	99.4	99.4	99.4	99.4	99.4	99.4	99.1	98.8	
Allowed (%)	0.9	1.2	0.6	0.6	0.6	0.6	0.6	0.6	0.9	1.2	
Outliers (%)	0	0	0	0	0	0	0	0	0	0	
Rotamer outliers (%)	0	0	2.54	1.12	0.87	0.86	1.81	1.39	0.76	0.69	
Clashscore	0.76	1.51	2.13	2.28	2.03	2.65	2.15	4.49	2.85	3.11	
Average	21.5	20.92	19.02	18.79	18.04	19.08	19.44	19.55	22.95	9.88	
B-factor (Å ²)											
Macromolecules	19.43	19.14	17.11	16.99	16.18	17.19	17.55	17.73	20.99	8.95	
Ligands	18.01	16.17	17.48	12.72	13.56	17.7	17.35	18.26	17.1	6.82	
Solvent	33.82	32.71	32.34	31.27	30.7	31.88	31.62	32.52	38.09	16.58	

022
023
024

Supplementary Table2 - Eurofins scanEDGE kinase assay shows no inhibition greater than >35% at 10 μ M across a panel of diverse kinases

Compound Name	Entrez Gene Symbol	Percent Control
AVI-4206	ABL1	74
AVI-4206	ABL1	95
AVI-4206	ABL1	67
AVI-4206	ABL1	78
AVI-4206	ACVR1B	91
AVI-4206	CABC1	100
AVI-4206	AKT1	80
AVI-4206	AKT2	100
AVI-4206	ALK	69
AVI-4206	AURKA	95
AVI-4206	AURKB	77
AVI-4206	AXL	84
AVI-4206	BMPR2	92
AVI-4206	BRAF	70
AVI-4206	BRAF	99
AVI-4206	BTK	100
AVI-4206	CDK19	99
AVI-4206	CDK2	86
AVI-4206	CDK3	100
AVI-4206	CDK7	99
AVI-4206	CDK9	100
AVI-4206	CHEK1	90

AVI-4206	CSF1R	84
AVI-4206	CSNK1D	88
AVI-4206	CSNK1G2	97
AVI-4206	DCLK1	91
AVI-4206	DYRK1B	99
AVI-4206	EGFR	91
AVI-4206	EGFR	95
AVI-4206	EPHA2	100
AVI-4206	ERBB2	91
AVI-4206	ERBB4	100
AVI-4206	MAPK3	98
AVI-4206	PTK2	89
AVI-4206	FGFR2	100
AVI-4206	FGFR3	97
AVI-4206	FLT3	97
AVI-4206	GSK3B	81
AVI-4206	IGF1R	100
AVI-4206	CHUK	82
AVI-4206	IKBKB	93
AVI-4206	INSR	68
AVI-4206	JAK2	94
AVI-4206	JAK3	93
AVI-4206	MAPK8	88
AVI-4206	MAPK9	73

AVI-4206	MAPK10	88
AVI-4206	KIT	100
AVI-4206	KIT	100
AVI-4206	KIT	89
AVI-4206	STK11	39
AVI-4206	MAP3K4	96
AVI-4206	MAPKAPK2	85
AVI-4206	MARK3	94
AVI-4206	MAP2K1	55
AVI-4206	MAP2K2	60
AVI-4206	MET	98
AVI-4206	MKNK1	68
AVI-4206	MKNK2	70
AVI-4206	MAP3K9	100
AVI-4206	MAPK14	99
AVI-4206	MAPK11	91
AVI-4206	PAK1	100
AVI-4206	PAK2	88
AVI-4206	PAK4	100
AVI-4206	CDK16	83
AVI-4206	PDGFRA	41
AVI-4206	PDGFRB	91
AVI-4206	PDPK1	85
AVI-4206	PIK3C2B	100

AVI-4206	PIK3CA	100
AVI-4206	PIK3CG	100
AVI-4206	PIM1	100
AVI-4206	PIM2	86
AVI-4206	PIM3	100
AVI-4206	PRKACA	84
AVI-4206	PLK1	86
AVI-4206	PLK3	90
AVI-4206	PLK4	91
AVI-4206	PRKCE	76
AVI-4206	RAF1	95
AVI-4206	RET	100
AVI-4206	RIOK2	61
AVI-4206	ROCK2	74
AVI-4206	RPS6KA3	67
AVI-4206	NUAK2	68
AVI-4206	SRC	82
AVI-4206	SRPK3	92
AVI-4206	TGFBR1	84
AVI-4206	TEK	100
AVI-4206	NTRK1	99
AVI-4206	TSSK1B	100
AVI-4206	TYK2	100
AVI-4206	ULK2	100

AVI-4206	KDR	45
AVI-4206	STK32C	85
AVI-4206	ZAP70	91

025
026
027

Supplementary Table3 Pharmacokinetic parameters for AVI-4206 following IV (10 mg/kg), PO (50 mg/kg), and IP (100 mg/kg) doses in male CD1 mice (n = 3 per group).

IV (10 mg/kg)			PO (50 mg/kg)			IP (100 mg/kg)		
parameter	units	value	parameter	units	value	parameter	units	value
CL	ml/min/kg	69.5	T _{max}	hr	1.0	T _{max}	hr	0.250
V _{ss}	l/kg	1.32	C _{max}	ng/ml	94.0	C _{max}	ng/ml	38067
T _{1/2}	hr	0.833	T _{1/2}	hr	4.69	T _{1/2}	hr	3.17
AUC _{last}	hr*ng/ml	2396	AUC _{last}	hr*ng/ml	433	AUC _{last}	hr*ng/ml	40998
AUC _{INF}	hr*ng/ml	2399	AUC _{INF}	hr*ng/ml	442	AUC _{INF}	hr*ng/ml	41003
MRT _{INF}	hr	0.316	F	%	3.69	F	%	171

028
029
030
031

Liver blood flow (mouse) = 120 ml/min/kg.

Supplementary Table4 - ADMET panel shows no antagonist response greater than >15% at 10 μM.

Assay	Ligand or Substrate	Antagonist Response at 10 μM
Cholinesterase, Acetyl, ACES	Acetylthiocholine	4.1
Peptidase Bleomycin Hydrolase (BLMH)	Met-AMC	-0.4
Peptidase, CAN1 (CANPL1, Calpain-1)	Casein-FITC	5
Peptidase, CTSB (Cathepsin B)	Boc-Leu-Arg-Arg-AMC	-17.5
Peptidase, CTSG (Cathepsin G)	Suc-Ala-Ala-Pro-Phe-AMC	-3.2
Peptidase, CTSH (Cathepsin H)	L-Arg-AMC	-13.7
Peptidase, CTSK (Cathepsin K)	Z-Phe-Arg-AMC	-5
Peptidase, CTSL (Cathepsin L)	Z-Phe-Arg-AMC	2.6
Peptidase, CTSS (Cathepsin S)	Z-Leu-Arg-AMC	-50.7
Peptidase, CTSL2 (Cathepsin L2)	Z-Leu-Arg-AMC	-1.2
Peptidase, CTSZ (Cathepsin Z)	Mca-Arg-Pro-Pro-Gly-Phe-Ser-Ala-Phe-Lys(Dnp)-OH	-7.1
Peptidase, Chymase	Suc-Ala-Ala-Pro-Phe-AMC	-5.1
Peptidase, Chymotrypsin	Suc-Ala-Ala-Pro-Phe-AMC	-0.7
Peptidase, Factor VIIa	N-CH ₃ -SO ₂ -D-Phe-Gly-Arg-pNA	-3.3
Peptidase Kallikrein Plasma	Z-FR-AMC	7.9
Peptidase, PLAU (Urokinase)	Z-Gly-Gly-Arg-AMC	11.2
Cyclooxygenase COX-1	Arachidonic acid	0.6
Cyclooxygenase COX-2	Arachidonic Acid	5.7
Monoamine Oxidase MAO-A	Kynuramine	3.3
Phosphodiesterase PDE3A	FAM-cAMP	0.6
Phosphodiesterase PDE4D2	FAM-cAMP	0.8
Peptidase, CASP2 (Caspase 2)	Z-VDVAD-AFC	4.1
Peptidase, CASP4 (Caspase 4)	Ac-LEVD-AFC	-2.9

Peptidase, CASP5 (Caspase 5)	Ac-WEHD-AFC	-6.6
Peptidase, Prolyl Oligopeptidase (POP)	Z-Gly-Pro-AMC	-0.5
Peptidase, Plasmin	H-D-Val-Leu-Lys-pNA	-1.5
Peptidase, Thrombin	Z-Gly-Pro-Arg-AMC	0.4
Peptidase, Tissue Plasminogen Activator (tPA)	N-alpha-Z-D-Arg-Gly-Arg-pNA	1.5
Peptidase, Trypsin	Z-Gly-Pro-Arg-AMC	-1.6
Peptidase, Tryptase	Z-Gly-Pro-Arg-AMC	-0.5
Peptidase, ELA2 (Neutrophil Elastase 2)	N-MeOSuc-Ala-Ala-Pro-Val-pNA	-3
Peptidase, ELA1 (Pancreatic Elastase 1)	N-MeOSuc-Ala-Ala-Pro-Val-pNA	-2.2
Protein Tyrosine Kinase, LCK	Poly(Glu:Tyr)	-1.4
Peptidase, Dipeptidyl Peptidase 4 (DPP4, DPP IV)	GP-AMC	1.3
Peptidase, CASP1 (Caspase 1)	Z-YUAD-AFC	-0.9
Adenosine A2A	[3H]CGS-21680	-1
Adrenergic alpha1A	[3H]Prazosin	2.1
Adrenergic alpha2A	[3H]Rauwolscine	4.9
Adrenergic beta1	[125I]Cyanopindolol	2.4
Adrenergic beta2	[3H]CGP-12177	-10.5
Transporter, Norepinephrine (NET)	[125I]RTI-55	-2.4
Androgen (Testosterone)	[3H]Methyltrienolone	-1.5
Calcium Channel L-Type, Dihydropyridine	[3H]Nitrendipine	-6.2
Cannabinoid CB1	[3H]SR141716A	4.2
Cannabinoid CB2	[3H]WIN-55,212-2	6.7
Cholecystokinin CCK1 (CCKA)	[125I]CCK-8	-6.9
Dopamine D1	[3H]SCH-23390	-12.1

Dopamine D2S	[3H]Spiperone	-15.8
Transporter, Dopamine (DAT)	[125I]RTI-55	6
Endothelin ETA	[125I]Endothelin-1	3
GABAA, Flunitrazepam, Central	[3H]Flunitrazepam	-9.9
Glucocorticoid	[3H]Dexamethasone	6.9
Glutamate, NMDA, Agonism	[3H]CGP-39653	-2.9
Histamine H1	[3H]Pyrilamine	-12.8
Histamine H2	[125I]Aminopotentidine	2.5
Muscarinic M1	[3H]N-Methylscopolamine	-8.1
Muscarinic M2	[3H]N-Methylscopolamine	-0.4
Muscarinic M3	[3H]N-Methylscopolamine	-2.6
Opiate delta1 (OP1, DOP)	[3H]Naltrindole	-3.2
Opiate kappa (OP2, KOP)	[3H]Diprenorphine	6.3
Opiate mu (OP3, MOP)	[3H]Diprenorphine	8.2
Potassium Channel [KA]	[125I]alpha-Dendrotoxin	5.6
Potassium Channel hERG, [3H]Dofetilide	[3H]Dofetilide	-4.7
Serotonin (5-Hydroxytryptamine) 5-HT1A	[3H]8-OH-DPAT	-2.3
Serotonin (5-Hydroxytryptamine) 5-HT1B	[3H]GR125743	2.2
Serotonin (5-Hydroxytryptamine) 5-HT2A	[3H]Ketanserin	8.3
Serotonin (5-Hydroxytryptamine) 5-HT2B	[3H]Lysergic acid diethylamide (LSD)	-4.5
Serotonin (5-Hydroxytryptamine) 5-HT3	[3H]GR-65630	-3.2
Transporter, Serotonin (5-Hydroxytryptamine) (SERT)	[3H]Paroxetine	-2.2
Sodium Channel Nav1.5	[3H]BNZA	0.3
Vasopressin V1A	[125I]PhenylacetylTyr(Me)PheGlnAsnArgProArgTyr	2

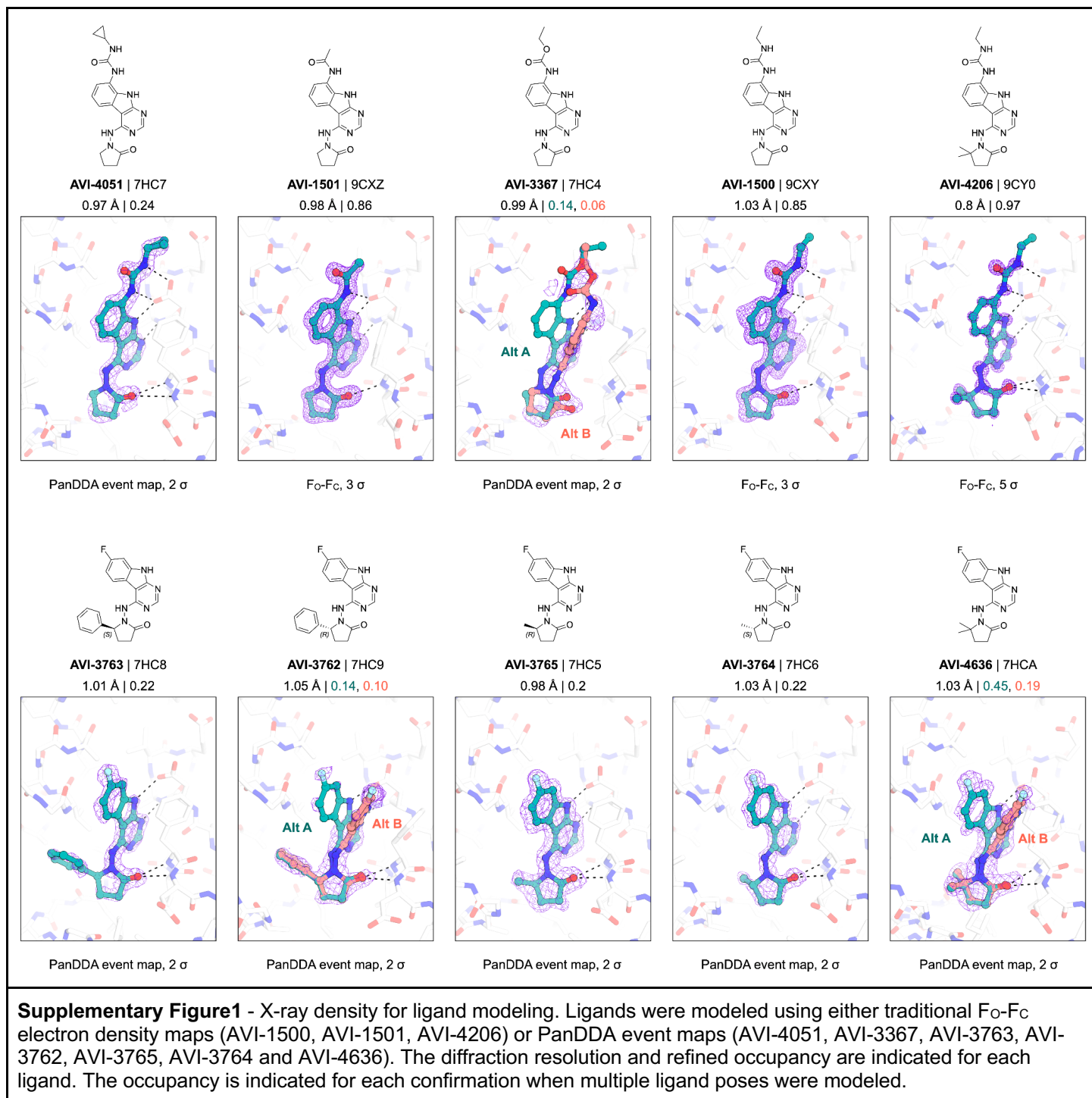
Nicotinic Acetylcholine alpha4beta2, Cytisine	[3H]Cytisine	4.7
---	--------------	-----

032
033
034
035

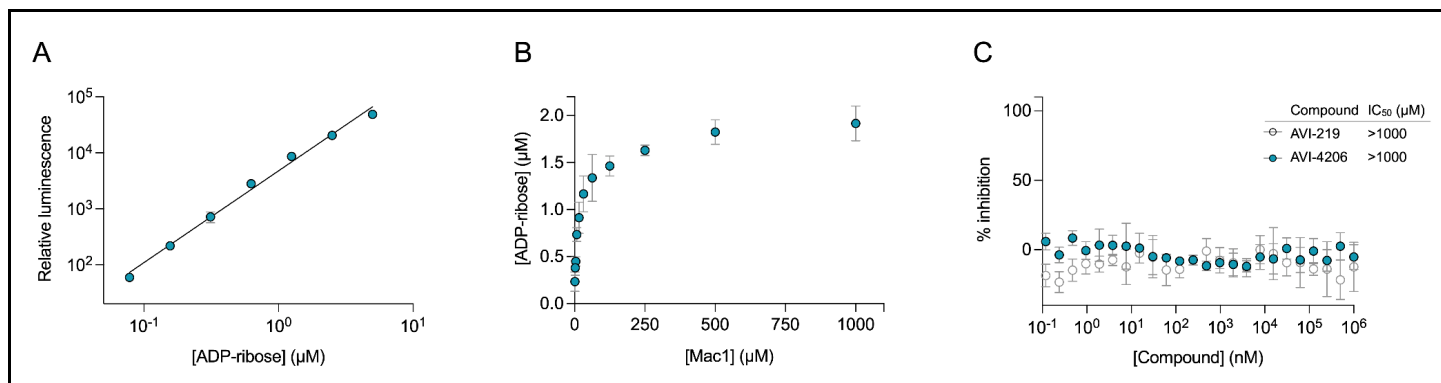
Supplementary Table5 Macrodomain protein sequences

Protein	Use	Sequence
hMacroD2	HTRF	MHHHHHSSGVDLGTENLYFQSYPSNKKKKVWREEKERLL KMTLEERRKEYLRDYIPLNSILSWKEEMKGGQNDDEENTQE TSQVKKSLTEKVS LYRGDITLLEVDAIVNAANASLLGGGGVD GCIHRAAGPCLLAECRNLNGCDTGHAKITCGYDLPAKYVIHT VGPIARGHINGSHKEDLANCYKSSLKLVKENNIRSVAFPCIST GIYGFNPEPAAVIALNTIKEWLAKNHHEVDRIIFCVFLEVDKI YKKKMNEFFSVDDNNEEEEDVEMKEDSDENGPEEKQSVEE MEEQSQDADGVNTVTPGPASEEAVEDCKDEDFAKDENIT KGGEVTDHSVRDQDHPDGGQENDSTKNEIKIETESQSSYMET EELSSNQEDAVIVEQPEVIPLTEDQEEKEGKAPGEDTPRM PGKSEGSSDLENTPGPDAGAQAQDEAKEQRNGTKGLNDIFEA QKIEWHE
Targ1	HTRF	MHHHHHSSGVDLGTENLYFQSMASLNEDPEGSRITYVK GDLFACPKTDSLACISED CRMGAGI AVLFKKFGGVQELL NQKKSGEVA VLKRDGRYIY LITKKRASHKPTYENLQKSLE AMKSHCLKNGVTDLSMPRIGCGLDRLQWENVSAMIEEVFE ATDIKITVYTL
Mac1	HTRF	MSYYHHHHHLESTSLYKAGFLEVL FQGPEVNSFSGYLKL TDNVYIKNADIVEEAKKV KPTVVVNAANVYLKHGGGVAGAL NKATNNAMQVESDDYIATNGPLKVG GSCVLSGHNLA KHCL HVVGPNV NKGEDIQLLKSAYENFNQHEVLLAPLLSAGIFGAD PIHSLRVCVDTVRTNVYLAVFDKNLYDKLVSSFLEMKSEK
Mac1	CETS A	MDYKDHGDYKDHDIDYKDDDDKGGGSGGGSGGGSTIEV NSFSGYLKLT DNVIKNADIVEEAKKV KPTVVVNAANVYLKH GGGVAGALNKATNNAMQVESDDYIATNGPLKVG GSCVLSG HNLAKHCLHVVGPNV NKGEDIQLLKSAYENFNQHEVLLAPL LSAGIFGADPIHSLRVCVDTVRTNVYLAVFDKNLYDKLVSSF LEMKGSVSGWRLF KKISGSEGRSLLTCGDVEENPGPMVS ELIKENMHMKLYMEGTVNNH HFCTSEGEKPYEGTQTMRI KAVEGGPLPFAFDILAT SFMYGSKTFINHTQGIPDFFKQSFP EGFTWERVTTYEDGGVLTATQDTS LQDGLIYNVKIRGVNF PSNGPVMQKKT LGWEASTETLYPADGGLEGRADMALKLVG GGHLICNLKTTYRSK KPAKNLKM PGVYVDRRLERIKEADK ETYVEQHEVA VARYCDLPSKLGHR*

036
037



Supplementary Figure1 - X-ray density for ligand modeling. Ligands were modeled using either traditional Fo-Fc electron density maps (AVI-1500, AVI-1501, AVI-4206) or PanDDA event maps (AVI-4051, AVI-3367, AVI-3763, AVI-3762, AVI-3765, AVI-3764 and AVI-4636). The diffraction resolution and refined occupancy are indicated for each ligand. The occupancy is indicated for each conformation when multiple ligand poses were modeled.



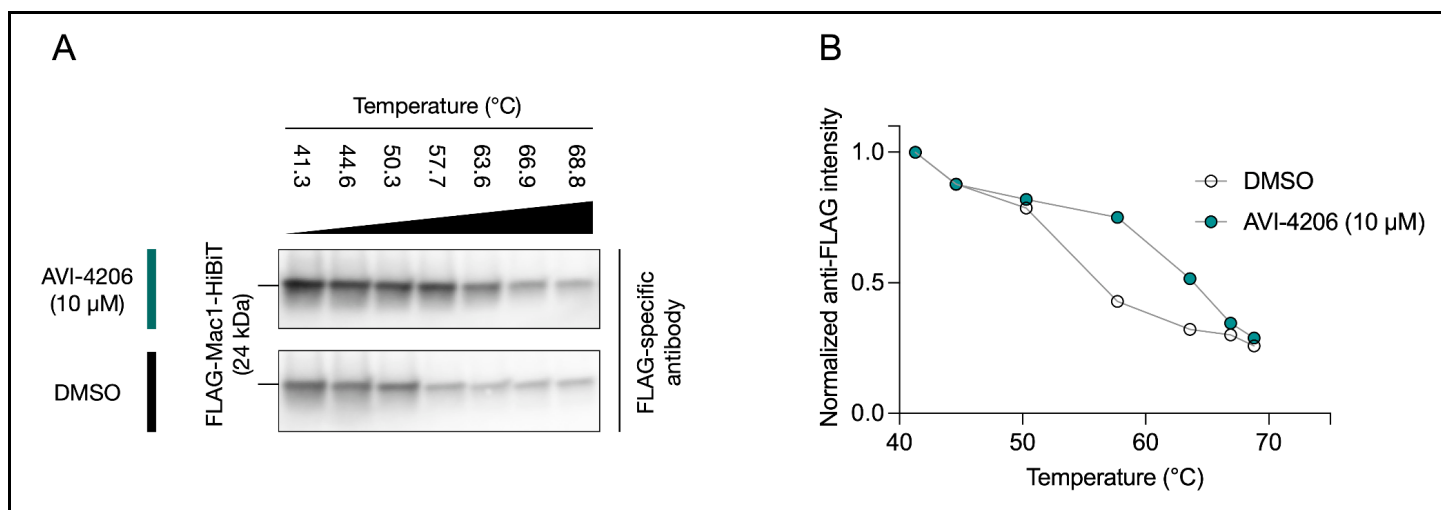
Supplementary Figure 2. AVI-4206 and AVI-219 inhibition of Mac1 determined using auto-mono-ADP-ribosylated PARP10 as a substrate.

(A) Standard curve of ADP-ribose detected using 100 nM NUDT5 and the AMP-Glo assay kit. Data are presented mean ± SD for four technical replicates. Data were fitted with a power function in the form $y = kx^a$ using non-linear regression (gray line).

(B) Titration of Mac1 with auto-mono-ADP-ribosylated PARP10. The concentration of PARP10 was 10 μM based on absorbance at 280 nm, but the titration indicated that the concentration of ADP-ribose released by Mac1 was five-fold lower (~2 μM). Data are presented mean ± SD for four technical replicates.

(C) Counterscreen of compounds against 100 nM NudT5 with 2 μM ADP-ribose as a substrate. No inhibition was detected up to 1 mM compound. Data are presented mean ± SD for four technical replicates.

039

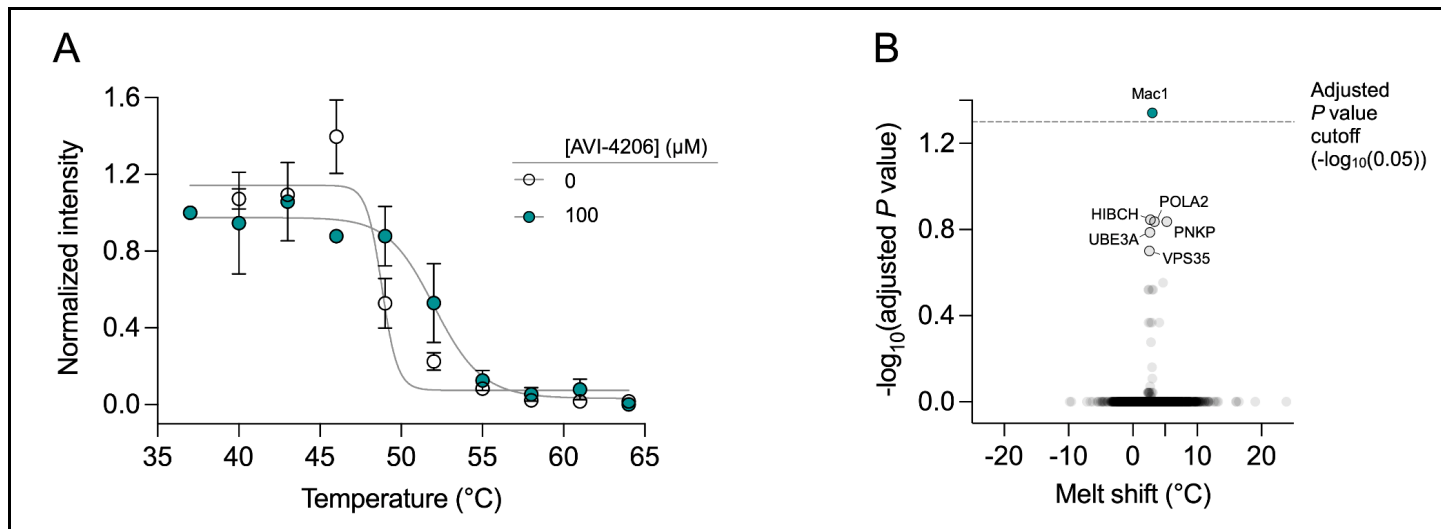


Supplementary Figure 3: AVI-4206 increases thermal stability of Mac1 in cells.

(A) CETSA-WB shows thermal stabilization of FLAG-tagged Mac1 protein after treatment of A549 cells with 10 μM of AVI-4206.

(B) Densitometry values were normalized to the lowest temperature for each treatment. Data are presented as a single densitometry measurement.

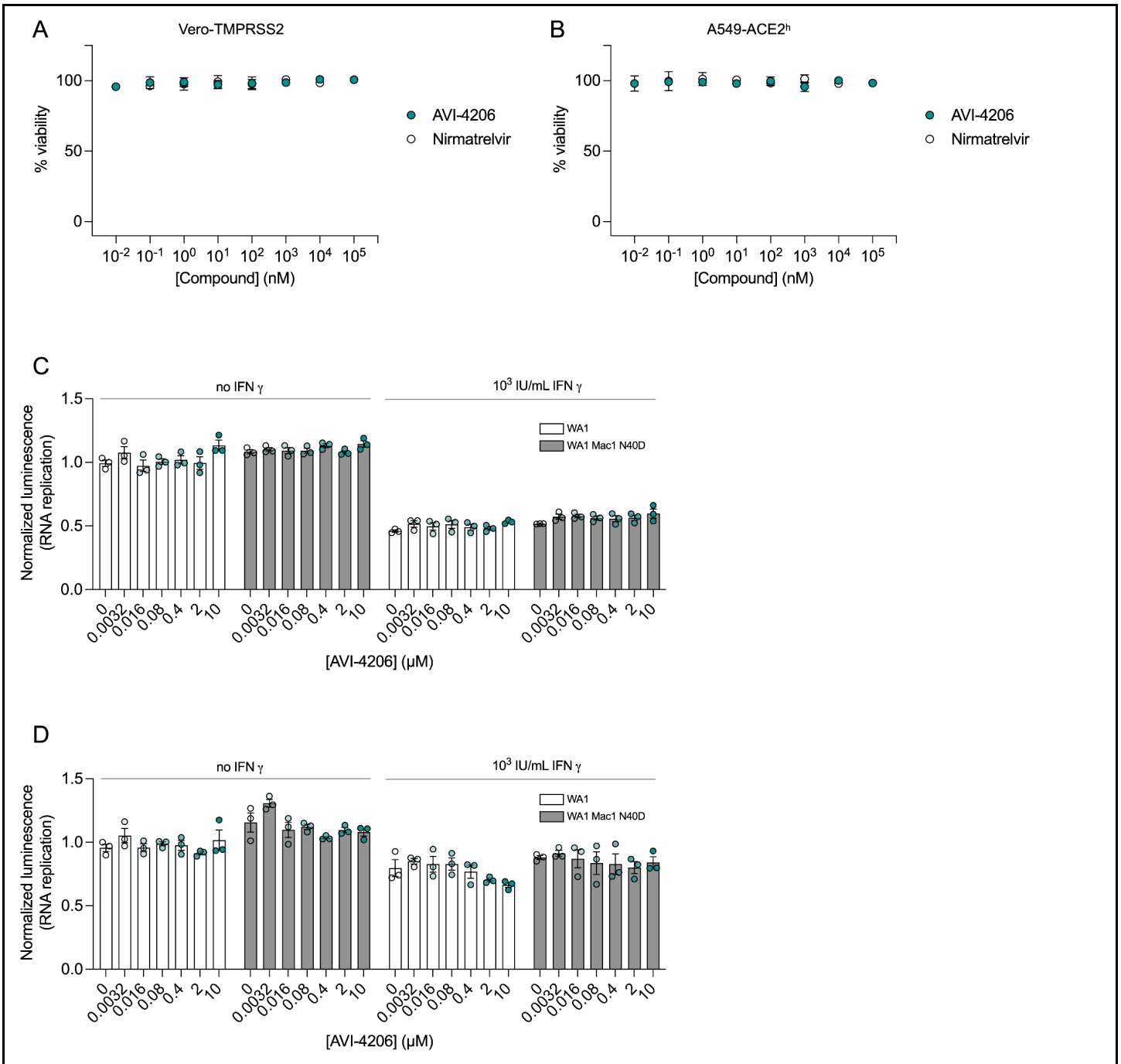
040
041



Supplementary Figure4: Thermal proteome profiling in A549 cellular lysates.

(A) Melting curve for Mac1 in A549 lysates treated in duplicate with either DMSO or 100 μM of AVI-4206. Data were normalized to the mean intensity at 37°C. Data were fitted with a sigmoidal dose-response equation using non-linear regression (gray line).

(B) Volcano plot of the statistical significance and degree of melting temperature shift for all proteins with high quality melting curves ($n = 3,446$ proteins). Teal circles indicate proteins with a statistically significant shift in melting temperature (adjusted P value < 0.05). The highest non-significant proteins are labeled and do not have obvious functional overlap with macrodomains.



Supplementary Figure 5: AVI-4206 has limited antiviral efficacy and no cytotoxicity in cellular models of infection.

(A and B) Drug cytotoxicity of AVI-4206 in Vero-TMPRSS2 (A) and A549 ACE2^h (B) was measured using the CellTiter-Glo® viability assay. Graphs represent the mean \pm SD of three biological replicates each conducted in triplicate.

(C and D) Luciferase readout of VAT (C) and A549 ACE2^h (D) cells infected with WA1 or WA1 Mac1 N40D replicons and treated with or without AVI-4206 and IFN- γ at indicated concentrations. Results are plotted as normalized mean \pm SD luciferase values of a representative biological experiment containing three technical replicates.

043
044
045
046
047

